NANOGAP ELECTRODE SENSOR FOR SINGLE ULTRAFINE PARTICULATE MATTER BY ELECTROMIGRATION

LAI KA HEI

MPhil

The Hong Kong Polytechnic University

2022

The Hong Kong Polytechnic University

Department of Applied Physics

NANOGAP ELECTRODE SENSOR FOR SINGLE ULTRAFINE PARTICULATE MATTER BY ELECTROMIGRATION

Lai Ka Hei

A thesis submitted in partial fulfilment of the requirements

for the degree of Master of Philosophy

August 2021

Certificate of Originality

I hereby declare that this thesis is my own work and that, to the best of my knowledge and belief, it reproduces no material previously published or written, nor material that has been accepted for the award of any other degree or diploma, except where due acknowledgement has been made in the text.

_____ (Signature)

Lai Ka Hei (Name of candidate)

Abstract

Ultrafine particulate matter is a mixture of liquid and solid particles with 100nm or less diameter. The insignificant size and mass, the high toxicity, and surface area per mass of ultrafine particulate matter have been thoroughly investigated and are more dangerous than larger particulate matter. The smaller aerodynamic diameter allows ultrafine particulate matter to penetrate deeper into alveoli and blood, leading to high blood pressure, ischemic and stroke. Therefore, the characterization and measurement of ultrafine particulate matter is key to understanding and reducing the risk of particles' exposure. Characterization of ultrafine particulate matter by transmission electron microscopy is profoundly used in research for understanding the model of ultrafine particulate matter, there is still lacking measurement methods and standards due to the limitation of commercial optical sense and Mie's theory. To fill the research gap, this work proposed to construct a new electrical sensing method by using nanogap electrode and metal-particle-metal configuration to measure the electrical signal of single ultrafine particulate matter. Electromigration and E-beam lithography is used to fabricate nanogap electrode. Keithley 2400 and the self-made programme is used for electrical measurement. The result of electrical signal was being compared with commercial optical sensor based on weather condition. Three implications can be derived from the electrical signal analysis: the number of counting particulate matter, the amplitude of current spike, and the morphology of current spike. The result is matched the relative humidity and weather information. This work starts a new chapter in detecting single ultrafine particulate matter by electrical measurement.

Acknowledgements

I would like to express my greatest gratitude to my supervisor, **Dr. ZHAO Jiong,** for his continued, professional guidance and support in these two memorable years. His door is always opened for us to have an extremely useful discussion. His enthusiasm and insightful suggestions always inspire me to pursue a higher standard.

Thanks for my co-supervisor, **Prof. YAN Feng** for his encouragement and suggestions.

Furthermore, I would like to acknowledge **Dr. LY Thuc Hue** and her group especially **Dr. YANG TieFeng** for their discussion and sharing the research skills to me.

Thanks all the technicians in the Department of Applied Physics and University Research facility in Materials Characterization and Device Fabrication (UMF) in Polyu, **Dr. LU Wei (CEM), Dr. Terence WONG** and **Ms. Joyce LAU (Cleanroom), Dr. Hardy LUI** and **Ms. Pendy HO (MRC), Dr. Pai WONG**, **Ms. Henrietta HO** and **Mr. CHAN Tsz Lam (AP)** for their training and maintenance all the laboratory in UMF and AP.

I would like to thank my research group for their altruistic and delightful help and support, including **Mr. Wong Lok Wing**, **Ms. ZHENG FangYuan, Mr. WONG Hok Yin** for their assistance and encouragement.

Additionally, special thanks to my dearest friends in PolyU, including **Mr. CHOY Tsz Hin, Mr. KAM Tsz Yau, Ms. LI Yuen Ling, Mr. Simon WONG** and **Mr. Dennis SUEN**. They always supported and shared their practical experience to finish this impossible MPhil study.

Dedicated to the memory of my grandmother, Ms. LEUNG Nga Tai, who encourage and guide me to be the right person.

Table of Contents

List of Figures

List of Tables

List of Publications

Fangyuan Zheng*, Wai Chung Lam*, **Ka Hei Lai***, Lingli Huang, Lok Wing Wong, Yisong Zhang, Zhangyuan Yan, Chak Chung Sham, Quoc Huy Thi, Thuc Hue Ly, and Jiong Zhao *Environmental Science & Technology Letters* **2020** *7* (8), 560-566

Chapter 1. Introduction

1.1. Background

The severe air pollution has brought many threats to human in terms of health, living environment and finance expenses [1-5]. In order to alleviate the risks caused by air pollution, the detection of various harmful vapours and gases becomes a critical area in research field. In 2016 the visibility of most of the cities in China had hit rock bottom due to the severe smog hazard [1, 2]. The alarming situation of air pollution in China has drawn great attention from worldwide to understand the effect of particulate matter (PM) [1, 2]. In this regard, research in single PM detection method and the respective correctness of the result becomes necessary. Among the various types of PM sensor, the optical sensor type based on Mie theory have been widely used because of the affordable cost, simple structure, and fast response [6]. Concerning the inaccuracy and limitation of optical sensor [3], it is of need to develop a new sensor with a different approach to detect PM especially the ultra-fine PM. Therefore, this work aims to construct a new electrical sensing method for ultrafine particulate matter (UFP) in a metal-particle-metal structure. In the metal-particle-metal structure (Figure 1), electrical signal can be used to characterize the property of the PM and count the number of PM. Due to the lack of electrical single PM particle sensing result, this work proposed to use gold nanogap electrode, fabricated by electromigration and e-beam lithography to achieve real-time single PM measurement and analyse the composition of PM by the electrical signal. It will be a new chapter for PM sensing.

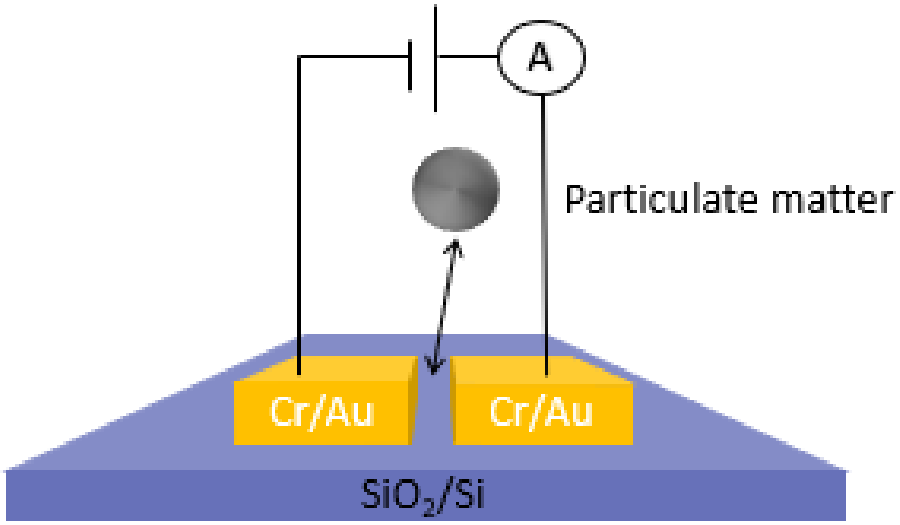

Figure 1. Schematic diagram of Metal-particle-Metal sensing of PM

1.2. Effect of Particulate matter

With the advance of science and technology, air pollution is still one of the serious problems which cannot be evaded[3]. Air pollution arises when the PM, a complicated mixture of liquid and solid particles, releases into the atmosphere that are detrimental to human health, environment, and economic activities[1-4] . According to the World Health Organization (WHO) in 2016[7], Particulate matter (PM) was 5th mortality risk factor in 2015 and 4.2 million to 8.9 million per year worldwide was killed as a result of absorption of PM into the lungs and bloodstream which increased the risk of asthma, cardiopulmonary disease, ischaemic heart disease and lung cancer[8]. Frequent human activities have worsened the severity of air pollution, 96% of the population lives are exposed to pollutant levels that are exceeding recommended limits.[9] PM also burdens the world economy, with an estimate 2-5% of global GDP is used to treat disease caused by air pollution.[10] The

effects of excessive PM (surface visibility, climate change and global radiation balance [2, 3]have attracted the world's attention.

1.2.1. Source of Particulate Matter

The sources of PM can be classified into two types, the primary one and the secondary one. The primary sources of PM are the PM emitted directly from anthropogenic, for example, combustion of fuel in transportation, industrial activities, chemical transformation [1, 3]. The primary sources also include natural sources, volcanic activities, sea spray and release of dust from living vegetation [11]. The secondary sources are the composition of nitrate, sulfate and / or organic matter. [12]. Secondary organic aerosol (SOA) involved complex physical and chemical processes [12] contributed a significant fraction (20-90%) of the mass for submicron particles.

1.2.2. Categories of Particulate matter

PM can be defined into three major sub-group according to its aerodynamic diameter: up to 10um (PM_{10}), up to 2.5um ($PM_{2.5}$), Up to 100nm ($PM_{0,1}$). In other words, PM_{10} is the group of PM consists of coarse PM (PM_{10}), fine PM ($PM_{2.5}$) and ultrafine fractions ($PM_{0,1}$), whereas $PM_{2.5}$ contains particles that is finer than the PM with aerodynamic diameter smaller than 2.5um. Different groups of PM will cause different degrees of damage to human body as finer PM will penetrate deeper in human body system and accumulate in core health system and vice versa. For example, the 5-10um particle will usually deposit on the upper airway and lung lymphatic [13], but the 1-2.5um particles accumulate in centrilobular emphysema through terminal bronchiole[14]. For UFP it will penetrate deeper to alveoli and blood to cause high blood pressure, ischemic and stroke and is expected to be more harmful to human[15, 16]. In this sense, among all pollutants, ultrafine

atmospheric aerosols heavily contribute to urban air pollution. Therefore, the large amount and pose health risks aroused researchers to find a way to understand UFP. [15, 16]

In addition to the size of PM, the surface-area to mass ratio helps to understand how the dynamic of UPM hinders the environment further. It has been a fact that air is mixed with all different sizes of particle, the total number and surface area of PM is dominated by UFP (Figure 2), UFP have an insignificant fraction of total mass therefore it has always been underestimated on its effect to the environment and health of human. The large surface-area to mass ratio and high surface reactivity[17, 18] (Figure 1) allows UFP to adsorb larger number of toxic substances per mass such as hazardous metal, and organic compound compared with fine PM and coarse PM[17, 18]. It is implied that UFP is more harmful to human than $PM_{2.5}$ However, due to instrumental limitations and the inability on characterization of UFP on the existing PM sensor, commercial sensors tend to focus on large particles rather than UFP[19] . There is no agreement for a standardized method and guidelines for measuring UFP and lack of a universal criterion of levels of air pollution in terms of UFP.

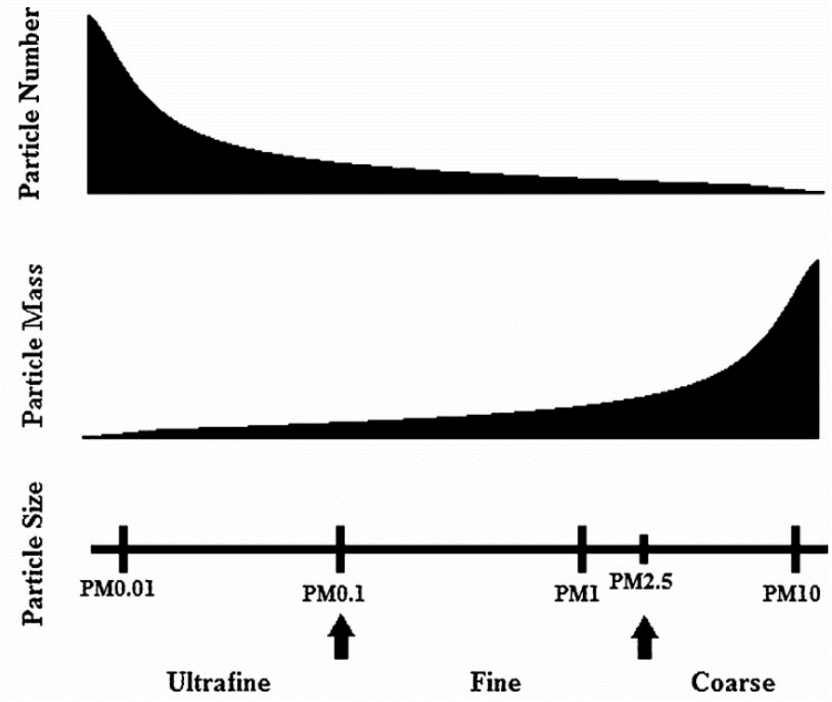

Figure 2. Theoretical distribution of Particular matter[18].

1.3. Single Particulate matter characterisation by Transmission electron microscopic

In a recent study, researcher introduced the use of transmission electron microscopy (TEM), scanning transmission electron microscopy (STEM), and chemical analysis for measurement of single PM with high-resolution structural and chemical information on the single-particle [20]. The recent advent of low-voltage and aberration-corrected TEM and STEM, [21] as well as multiple-detector EDS,[22] has achieved atomic resolution on the beam-sensitive specimens. The application of TEM and STEM in the study was a success in understanding the structure and composition of PM. The Core-shell structure (Figure 3) and composition (Figure 4) of hygroscopic secondary aerosols (SAs) is discovered by TEM and STEM [20]. The shells mainly consist of carbon (C), nitrogen (N), oxygen (O), and silicon (Si) in the outermost layers, whereas the inner cores contain N, O, sulfur (S), sodium (Na), potassium (K), and chlorine (Cl), with which the variable

component of salt can be mapped for comparison (Figure 4). These major elements are possibly contributed by the seawater cycle and the massive secondary photocatalytic reaction product, ammonia sulfate[32,33].[23] Other minor elements such as aluminum (Al), calcium (Ca), iron (Fe), magnesium (Mg), and zinc (Zn) are occasionally found in the cores.Also, Figure 5 showed the proportional relation between size of SAs and the O/C atomic ratio in the shell layer and influenced by the temperature.[20]

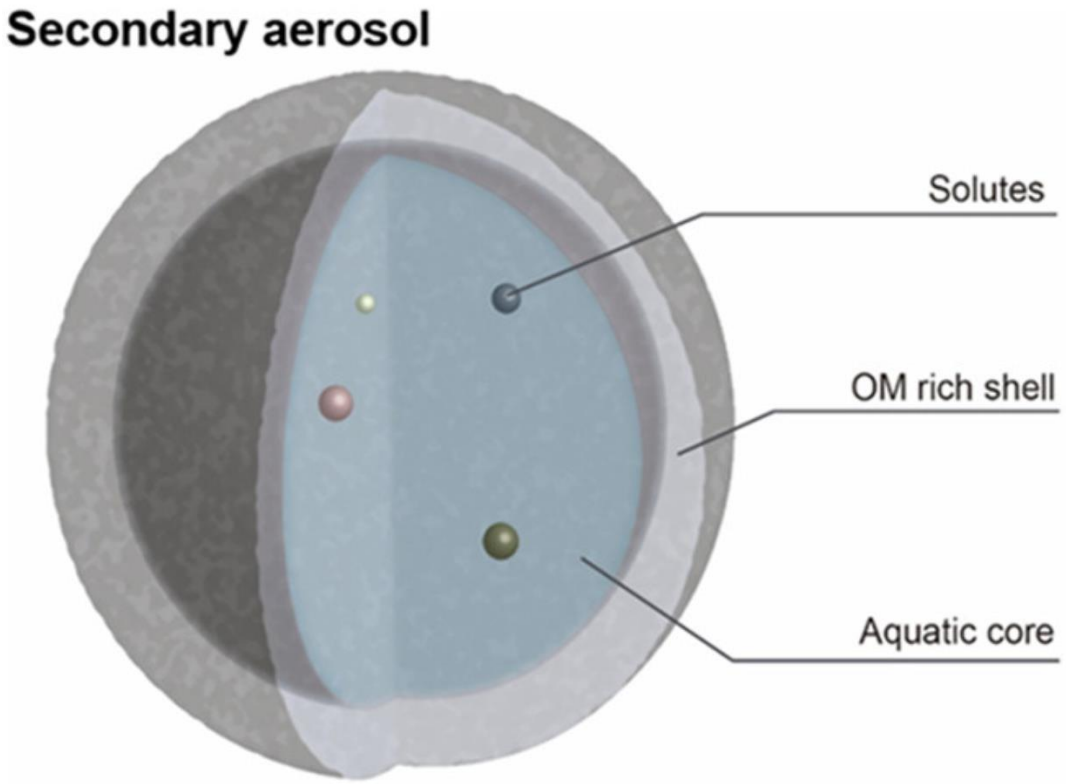

Figure 3. Illustration of the SAs[20].

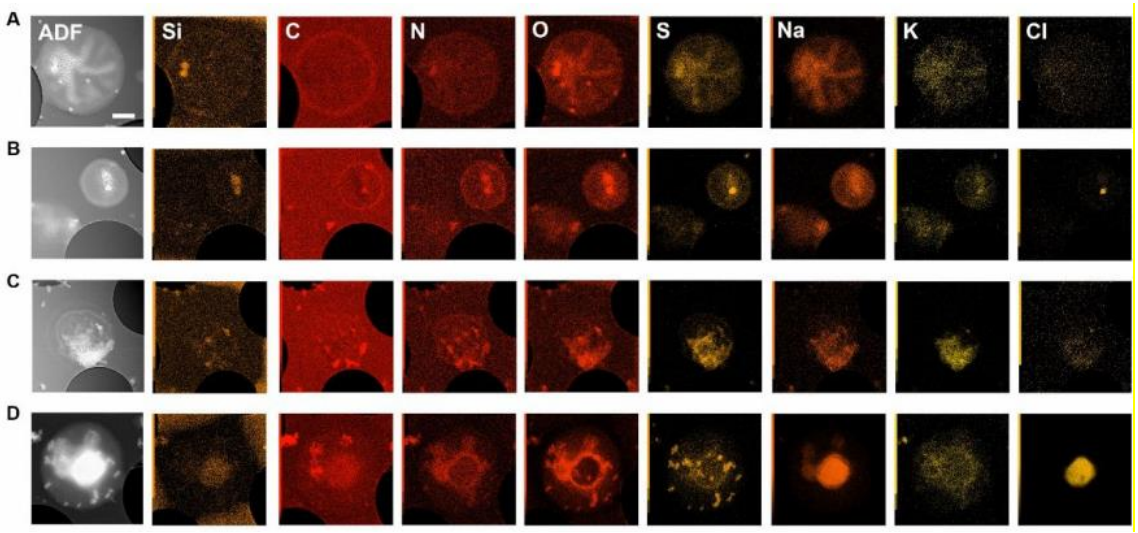

Figure 4. STEM -ADF and EDS mapping for single secondary aerosols[20].

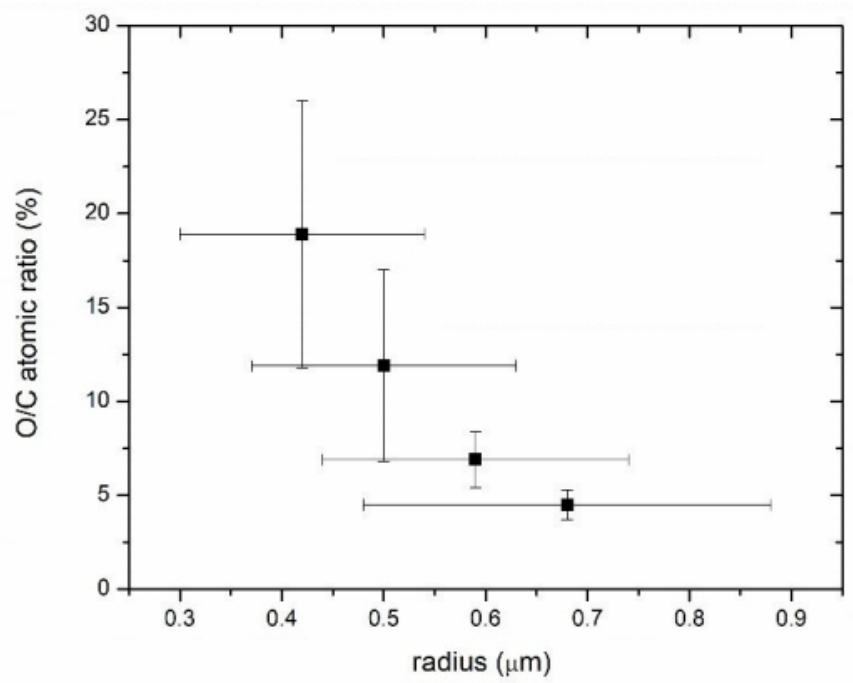

Figure 5. O/C atomic ratio versus radius of SA[20].

1.4. Objective

The objective of this study focusses on constructing a new electrical sensing method to quantifying single UFP by nanogap electrode. It will be a compactable, real-time single PM measurement, which is very important for human life and environment protection.

The major objectives are:

1) To analysis particulate matter property and chemical composition by Transmission electron microscopy.
2) To fabricate a new measurement device for Ultrafine PM.
3) To fabricate a nanogap by electromigration and construct a compact PM sensor.
4) To compare and modelling the measurement result with commercial optical measurement.

Chapter 2. Literature Review

2.1. Literature review of Particulate matter sensor

In response to the suggestions of deploying air quality monitoring station one pre square kilometre from WHO,[7] there is an urgent need for a compactable, portable and easy to use instrument to provide a real-time measurement of PM. However, Particulate matter contains a variety of chemicals which vary seasonally and regionally [1, 3], investigation of composition of pollutants is very complex.

Recently, PM is usually measured and recognized by size. There are currently two main types of commercial PM sensing technology: offline and real-time measurement. For offline measurement, TEM provides a very accurate chemical composition, size, and shape analysis. For real-time measurement, light-scatting particles sensor (LSPS) [24]and gravimetric measurement can measure PM in physics properties. The two measurements technology have been extensively used in commercial sector. Moreover, in the high-end laboratory setting, Tapered Element Oscillating Microbalance (TEOM) and Diffusion Size Classifiers (DiSC) are used as they offer a reasonable result of size and concentration of particles, but they are very expensive (>$20000usd)[6, 24]

3.2.1 Light-scattering Particle sensor (LSPS)

Light-scatting particles sensor is a low cost and compactable sensor commonly used for real time detection of PM in large scale. LSPS usually contain 3parts, a photodetector, a light source, and an air inlet. The principle of the LSPS is measuring elastic scattering of light on a spherical surface based on Lorenz-Mie theory[25]. Figure 6 demonstrated PM will pass through the laser and then the photodetector will receive

a signal peak proportional to particles size (absorbed light intensity and the scattering angle) [25]. However, this method is only accurate when the particles are much larger than the wavelength, and it is not appropriate for measuring the PM with size under micron size as it is harmful to human.[24] Although researcher used dual wavelength to solve this problem, it will require a complex and expensive components that are not cost-effective for such a low-cost sensor [26]. Also, Mie theory is restricted to spherical particles. The particles will not be a perfect and uniform sphere and bring inaccuracies to the measurement[19]. Also, the result of the sensor will be influenced by the temperature and relative humidity [27]. The light intensity is reduced when the water particle absorbs the initial light, therefore, the sensor will overestimate the particle concentration. [28] Another main error is LSPS is a coincidence error that occurs due to more than one particle present in the same light path simultaneously being counted to a one larger size or miscounted.

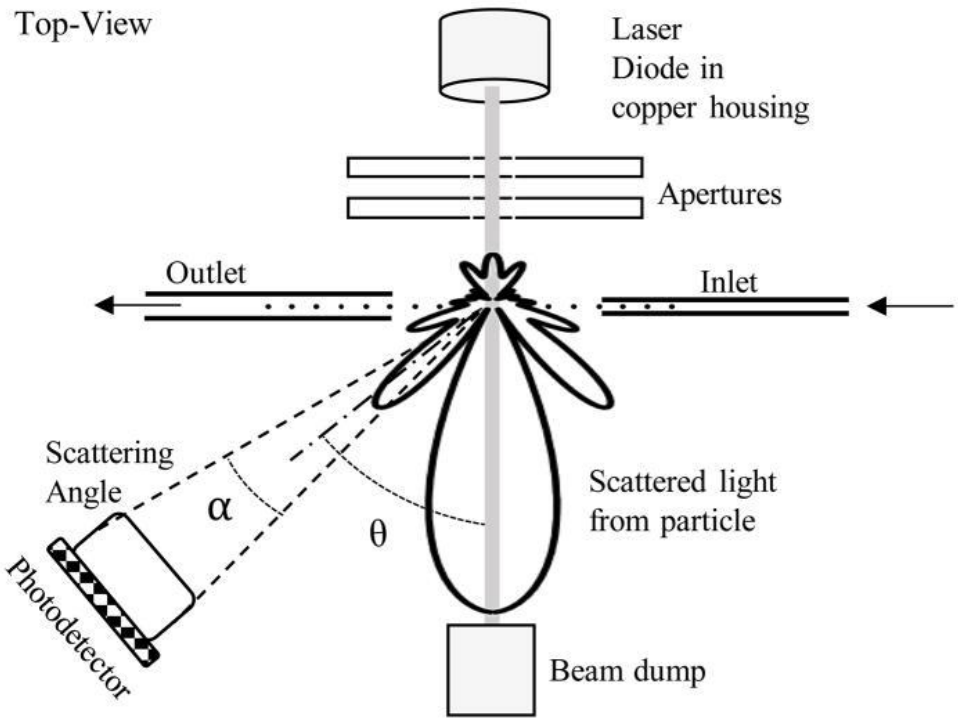

Figure 6 Schematic of LSPS. Reproduced from[25].

3.2.1.1 Light scattering Theory and characteristic

The first light scattering theory was developed in the 19th century by John Tyndall. Light scattering happened when the incident light wave collided with particles, the light(photons) will redirect to a new path. Elastic scattering appears when the wavelength of incident light is the same as scattered light. This phenomenon can be explained by the Mie theory, Ryleigh theory and geometry optics[29]. LSPS usually only uses Mie theory [19, 24]to predict the size of a particle according to the following formula[30]:

$$x = \frac{2\pi r}{\lambda} \; where \; x \; \approx 1 \qquad \textbf{Eq. 1}$$

$$I_S = \frac{\lambda^2 I_0}{4\pi R^2}\left(|S_1|^2 \sin^2\varphi + |S_2|\cos^2\varphi\right) \qquad \textbf{Eq. 2}$$

Where: x is size parameter, r is radius of the particles and λ is wavelength of incidence light. In Eq. 2, I_S is scattered light intensity, I_0 is incident light intensity, R is the distance between particle and observation point, S_1 and S_2 is the function linked to the scattering angle. Based on Mie theory, Eq.2 can be measured the intensity of scatting light when the optical plane wave collides a spherical particle.

3.2.2 Diffusion Size Classifiers (DiSC)

Since the drawback of LSPS is inextricability, current research has focused on electrical signal of the PM. Diffusion size classifier is introduced for measuring PM. The principle of DiSC is measuring the charge of the air based on unipolar and estimating particle concentration and the average size by the different filtering on the air.[31] Figure 7 shows DiSC usually contains 5 parts, a charger, an induction stage, an air inlet, a filter, and a diffusion stage. First, air is charged in the corona charger which is in high positive voltage and produced ion. Parts of the ion will attach PM in the air. The induction stage

and diffusion stage measure the current induced by the ion which is I_{Ind} and I_{diff}. Particle passing throught diffusion stage are collected in backup filter and measure current, which is I_{filt}. I_{filte} and I_{diff} are related to the large particles and smaller particles respectively, and the ratio of these current can estimate average particles size. Therefore, DiSC can measure the concentration of PM and separate different particles sizes[32]. DiSC has a lot of advantages, for example: high sensitivity (10nm -200nm), low power consumption and natural to weather and environmental factor. However, the manufacturing requires very high-end setting, the accuracy of measurement unit have to achieve fA level current[33]. The production cost is also expensive (~ $10000 usd). Moreover, the sensing area in DiSC must be cleaned frequently. Therefore, DiSC is not ideal for developing a personal and compact sensor.

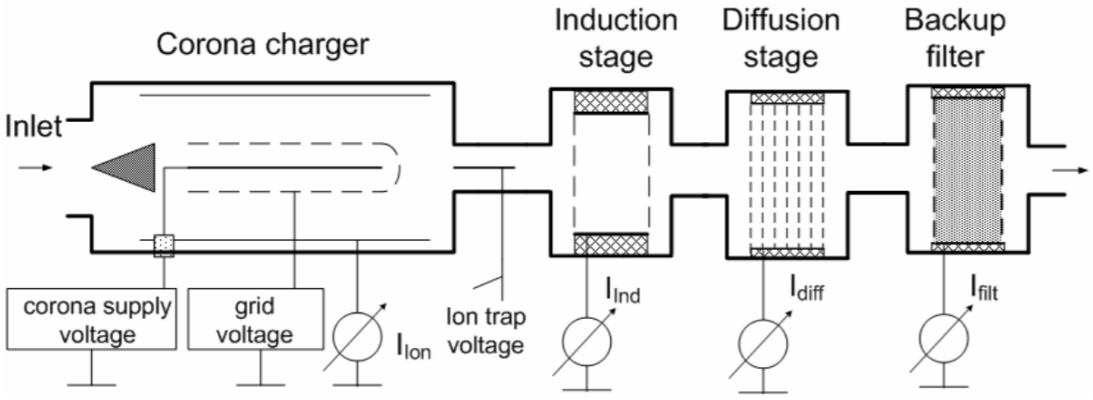

Figure 7 schematic of the DiSC. Reproduced from [31].

2.2. Electromigration

Electromigration is a phenomenon of atomic diffuse of the metals in conductor driven by currents, this phenomenon leads to formation of voids in cathode and hillocks in anode [34]. It can result in either: 1) open circuit if the voids formed to cut the metal line; or 2)

short circuit if the hillocks connect to another metal wire adjacent to it. Theory of electromigration is based on the unbalanced electrostatic force and electron-wind forces employed on metal ions. Electron interacting with an imperfect metal by electric field cause non-uniform and scattered distribution. Therefore, non-zero flux divergence occurs at the spot where the inequal number of atoms flowing in and out at that area pre time and causes the mass depletion or accumulation, formed of voids (Fig. 8) and hillocks (Fig. 9). Once a void forms, Joule heating and high current density will further accelerate growth of void because the reduced cross-sectional area of the conductor will increase the current density and cause current crowding around the void unit the void develops large enough to break down the metal line. This phenomenon can be modelled by the Black's equation:[35]

$$t_{50} = CJ^{-n}e^{-(Ea/kT)} \qquad \textbf{Eq. 3}$$

Where: t_{50} is median of failure time, C is constant, J is current density, n is the integer constant, T is temperature, k is the Boltzmann constant and Ea is activation energy. Therefore, by controlling the current density, nanogap (void) can be achieved by this simple useful technique.

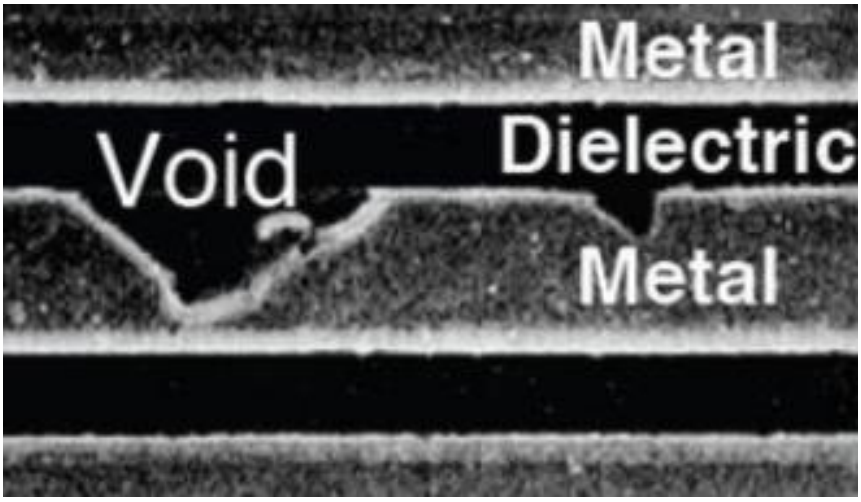

Figure 8. Formation of void[36].

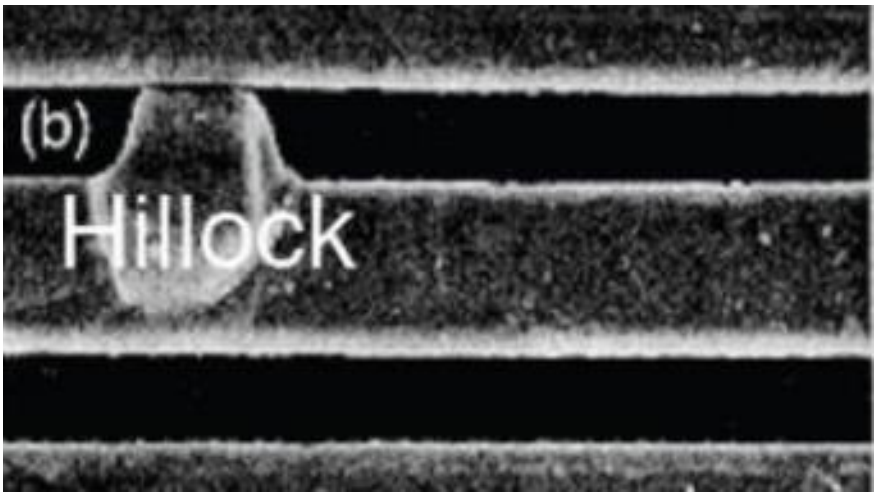

Figure 9. Formation of Hillock[36].

In recent research, there are several methods have been proposed to attain reproducible nanogaps by electromigration such as feedback control, self-breaking and current-voltage sweep.

In current-voltage sweep method, voltage sweeps by different ramp rate from 0V to reach certain current[23]. In Figure 10, maximum current point is set to 6mA. When the current reaches 6mA, voltage sweep from zero again until the resistance reaches 13 kΩ. 100 nm gap can be fabricated by this method (Figure 10b).

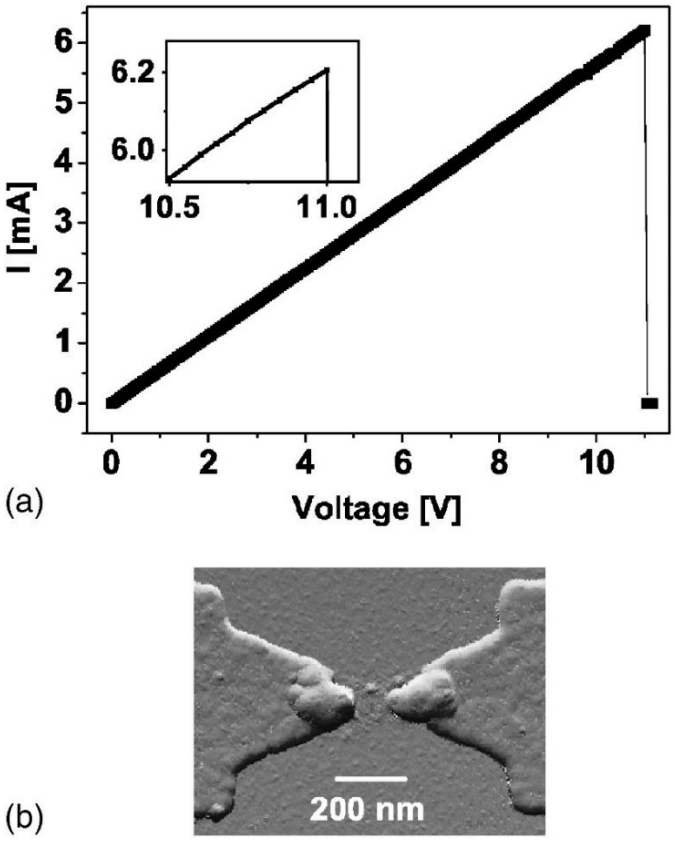

Figure 10. (a) Current-voltage measurement during current-voltage sweep method. (B) AFM images of the sample after electromigration [23].

In feedback control method, the resistance and current have been recorded during the cyclic voltage sweep[37]. When the voltage ramps up, the change of resistance has been controlled into 1-5% depends on the experiment and gap size. When resistance changes, the voltage will ramp down to control the resistance into 1-5% until resistance > 13 kΩ (Figure 11c) This method provides reproducibility than conductance method to obtain <1nm gap. Feedback control method was proposed by Strachan et al. they fabricated an Au bowtie structure by E-beam lithography and Johnston et al. demonstrated a reproducible and controllable nanogap in this method. These two methods will be used to this research. Except electromigration, there are serval methods to obtains nanogap such as mechanically controllable break junctions, crack-defined break junctions etc. Electromigration is the simple and controllable way to fabricate a nanogap.

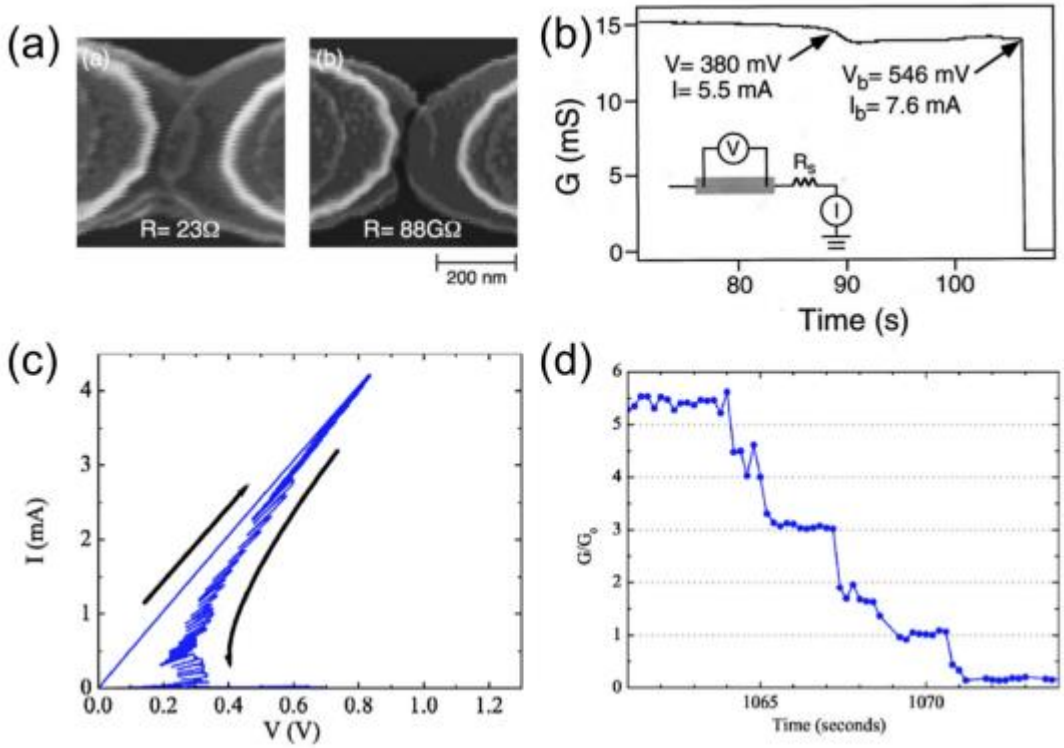

Figure 11. (a) SEM image of gold nanowire (a) before and (b) after. (b) the conductance-time curve during the feedback control method. The ramp rate is 30mV/s. (c) Current-Voltage curve of feedback control method. (d) The zoom of conductance of nanowire breaking down.[37]

2.3.Nanogap sensor

There are several methods for fabricating nanogap. In the past two decades, many nanogap fabricating technologies have been established [38]. The first nanogap technology device was introduced by US National Bureau of Standards [39] and adopted by Reed et al. [40]; In this device, elastic substrate containing piezoelectric material was fractured to form nanogap. Photolithography and electrodepositions have also been used to fabricate devices with around 10 nm gaps using electrochemical and chemical deposition processes[41]. However, due to nonuniformity, these approaches are unable to achieve gaps smaller than 10 nm. The sacrificial film technique can also be used to create nanogaps, however this method is limited to gaps larger than 50 nm [42]. The high uniformity and reproducible nanogap can be fabricated by electromigration [43].

The ability to measure and convert interactions of specific molecules into valuable electrical signals is the main advantage of these methods. The electrode structure and the use of sensing materials is open to modification is another effective method for improving sensor performance. Interdigitated electrode structures are often used in most resistive–type gas sensors, and the sensor response is mainly controlled by the interspacing between the electrode fingers, which is typically several microns. The application of nanogap devices to the detection of different gas and DNA sequencing[44], such as inorganic gases (H2 [45], [46], [47], CO [48],O_2 [49]and NO_2 [50]) and volatile organic compounds (acetone [51, 52] have been investigated. Previous research has demonstrated that reducing the gap separation between the electrode pairs improves the device's sensitivity [50, 52], limit of detection[45], and response speed. Mostly, nanogap device can be divided into 2 types: in-plane and out-plane.

DNA sequencing device by Tsutsui et al[44] developed a nanopore device by electromigration and RF sputtering is the traditional in-plane device. The sandwiches structure of SiO_2/Au/SiO_2 created a nanopore can be used to sequencing DNA through the electrical detection of single molecules. The voltage was hold on 0.75V and measured the current changes (Figure 12d) when the DNA solution injected to the channel. The current spike (I_p) indicated to single molecule trapping/ detrapping event in the nanopore. The low current and high current represented thymine(T) and guanine (G) in the oligomer respectively. Therefore, the DNA sequence can be determined by the current-time curve.

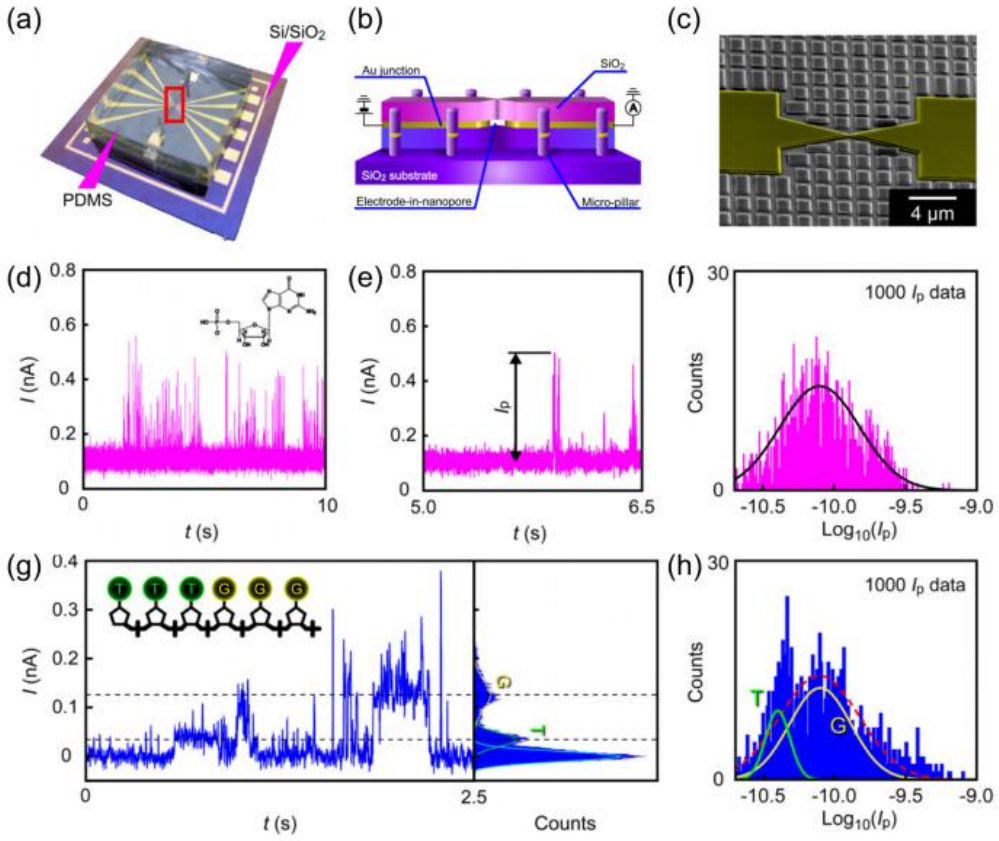

Figure 12. (a-c) Schematic image of DNA sequencing device. (d-e) Current-time curve measured when the DNA through the electrode. (f-h) Statistical histogram of the result.

Large scale of out of plane nanogap device was introduced by Nguyen et al[51]. The microlithography and etching methods allow full wafer-scale measurement. Nguyen proposed measuring the change of the capacitance can be detect acetone with a large range from 1000ppm to 100ppm. The top and down structure created a nanogap for acetone interaction. They record the change of capacitance, temperature, and acetone concentration in the chamber. Figure 13A shows the result during the experiment and Figure 13B shows the filtered result and the change of capacitance trails the acetone concentration very well. However, all the nanogap sensor also faced the same problem which is the area of the nanogap is small and restricted the sensitivity.

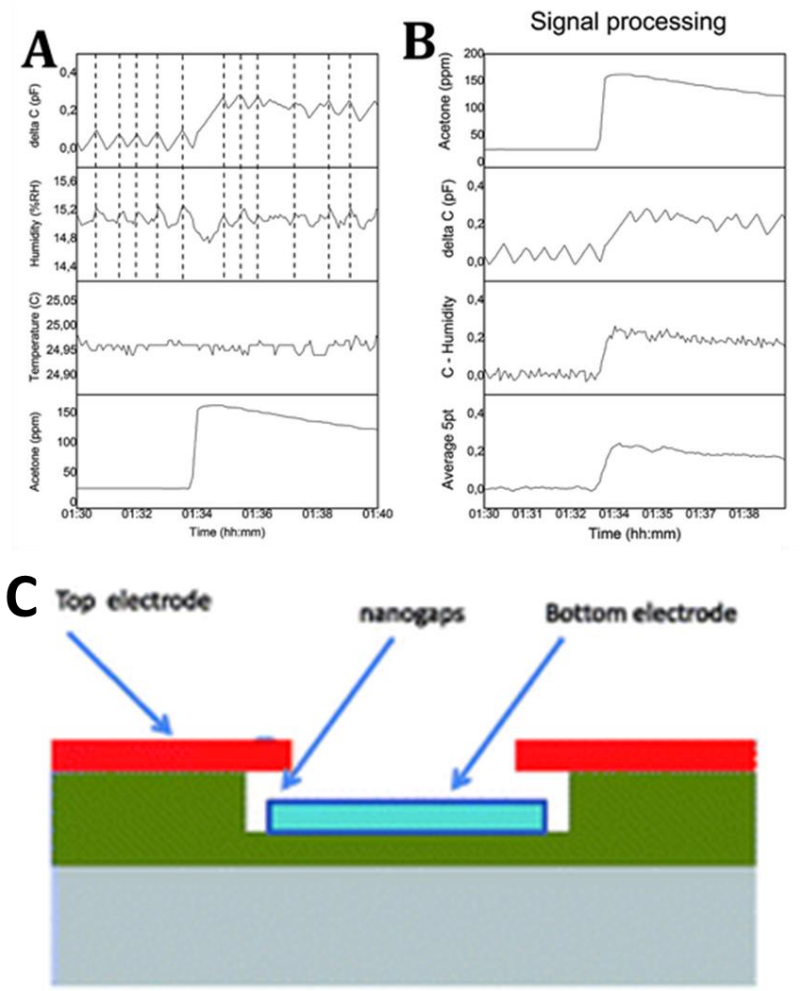

Figure 13. (a-b) Signal in acetone sensing experiment. (c) the schematic structure of acetone nanogap sensor [51]

Chapter 3. Methodology

Methodology will be divided to 2 parts which is fabrication of the Sensor and sensor testing.

3.1. Fabrication of Single Particulate Matter Sensor

The sensor involved a case, PM sensor chip, PCB board which used to support the PM sensor chip and pump.

3.1.1. Case of the Single Particulate Matter Sensor

The reason for manufacturing an outer case is to create a protection and an airtight space for PM sensor and therefore the airflow can be controlled by the pump. The outer case of PM sensor was made by the convenient and efficient 3D-printer. First, SOLID-WORK was used to design the case, then Formlabs Form 3 and Low force stereolithography (LFS) 3D printing technology uses laser, lens, and flexible resin tank to print 2 half cases from liquid resin. LFS technology and resin provide a compressive strength and high durability features. The design and the actual product illustrated in Figure 14 and Figure 15 respectively. Screws and nuts were used to combine the 2 half cases. Silicon O-ring was compressed by screw and nut to prevent air leakage. The width, length and height of airtight space was 20*80*30mm respectively. The diameter of inlet and outlet air was 15mm.

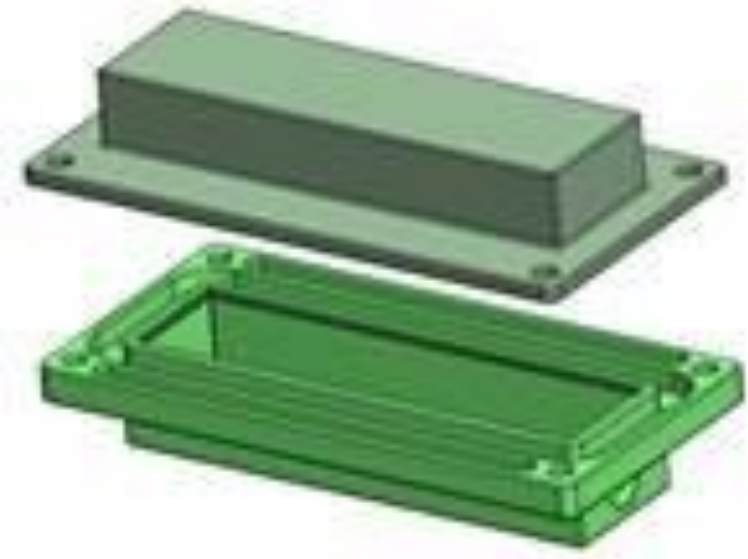

Figure 14. Schematic diagram of PM Sensor by SOLIDWORK.

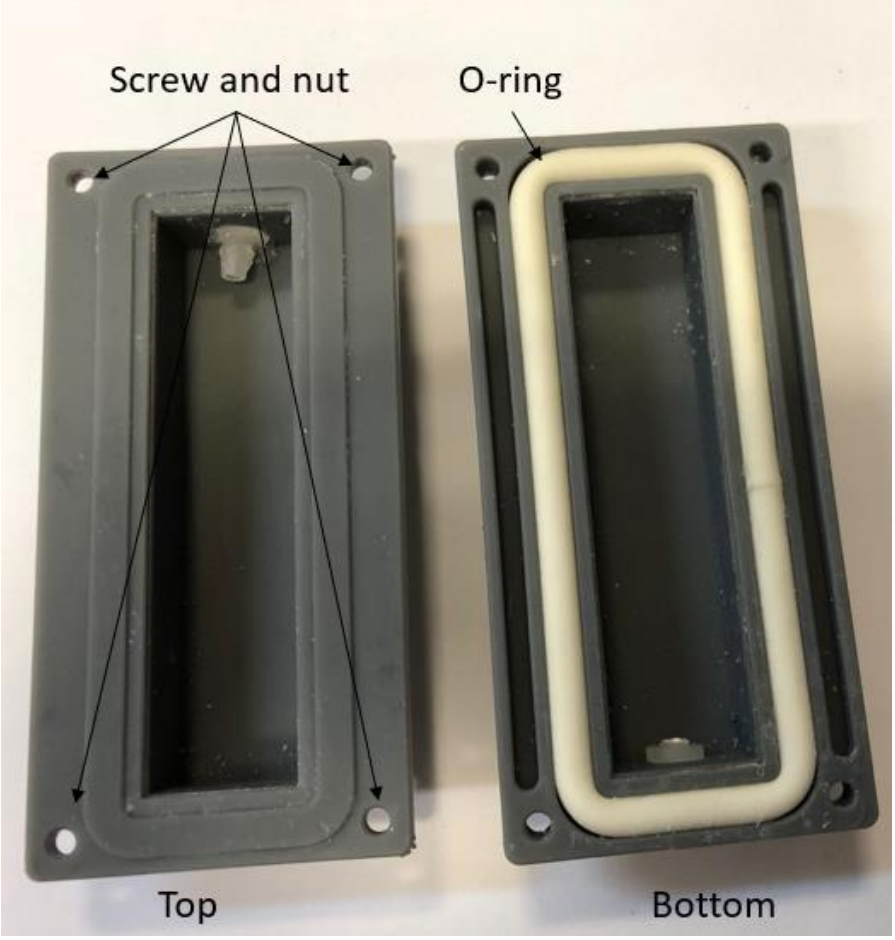

Figure 15. Actual product of PM sensor's case by LFS.

3.1.2. Single Particulate matter device

Figure 16 showed the schematic diagram of device fabrication. The 300nm SiO_2/Si wafer was used as the substrate. The SiO_2/Si wafer was cleaned by ultrasonication in acetone, isopropyl alcohol, and deionized water for 15 mins per solution. PMMA (A4,950K) was spin-coated on the SiO_2/Si at 4000 rpm for 60s and baked 160oC for 5 mins. The thickness of PMMA was around 200nm. AutoCAD was used to write a nanowire and 2 electrodes. JEOL JIB-4501 and nano pattern generation system(NPGS) was used to exposure the pattern written by AutoCAD. The dose was set to 210 uC/cm^2 and the beam current is 125 pA. After exposure, methyl isobutyl ketone and isopropyl alcohol with the ratio 1:3 were used to develop the pattern for 30s. Then, E-beam evaporation (Denton explorer E-beam deposition system) was used to deposit 5/50nm in 0.8 Å /s rate; Cr/Au on the patterning and lift-off by sonication with acetone to remove PMMA and washed by isopropyl alcohol and deionized water. After lift-off, nanowire was fabricated. Wire bonding (F&K Delvotec 5630 semi-automatic wire bonder system) was used to connect the electrode on the pattern and the PCB board. After that, Keithley 2400 and self-made LabVIEW program were used to perform the electromigration to produce a nanogap electrode. The details of electromigration are shown in Chapter 3.1.3. After electromigration, scanning electron microscope (Tescan VEGA3) was used for morphological inspection of nanogap. Then, the SiO_2/Si placed to PCB board and used wire-bonding to connect the electrode and PCB again. Finally, PCB with nanogap electrode was used to measure single PM.

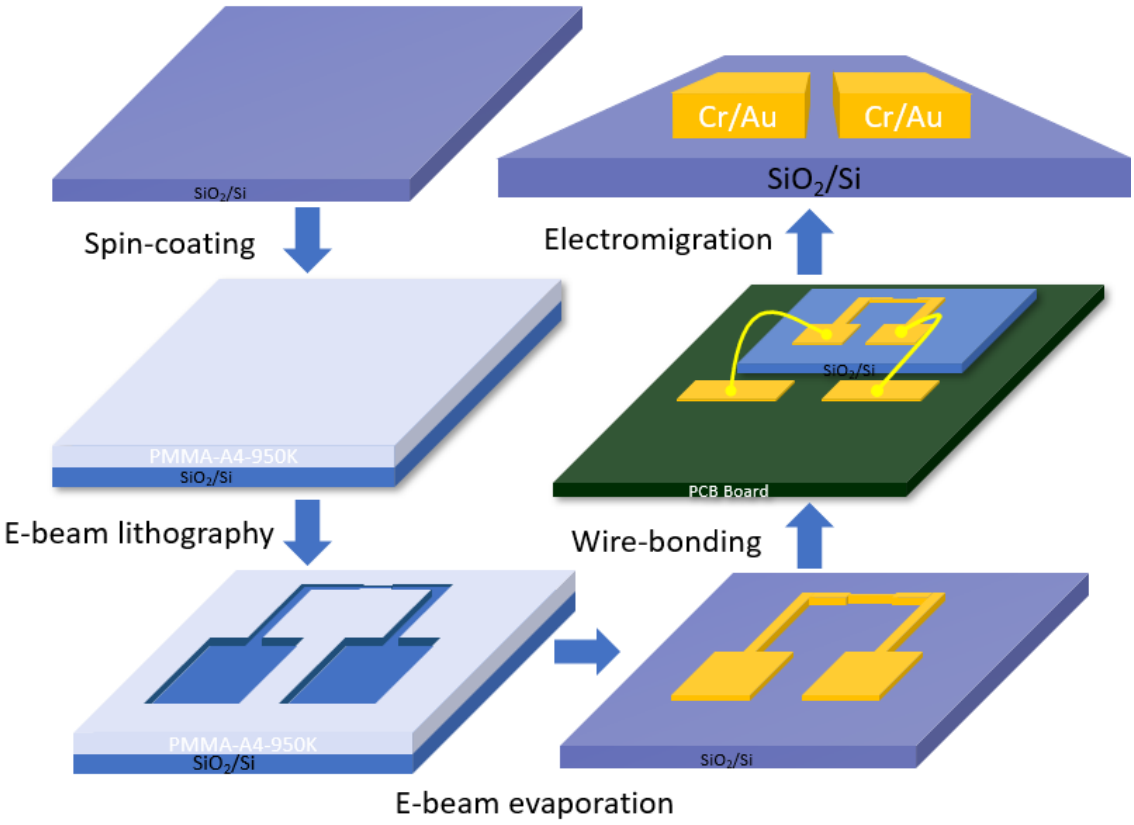

Figure 16. Schematic diagram of Device fabrication.

3.1.3. Nanogap fabrication by electromigration

After fabricate nanowire, nanogap were fabricated by electromigration by Keithley 2400 and self-made LabVIEW programme. Two different methods were used to fabricate nanogap: current voltage sweep and resistance feedback methods. The resolution of Keithley 2400 is 1pA and the time of each step is 0.1s.

For current-voltage sweep, a low voltage swept with constant ramp rate and measured the current at the same time and the current was limited to a constant. The flow chart was detailed in Figure 17. After the current reached the limit, when there was no increment in resistance, the step repeated with a current limit increased by 10%. If there was

any resistance increasement no changes to the current limit were observed, and the voltage sweep would start again. The result implied that the electromigration took place. Finally, repeat IV Sweep until the resistance reached 13kΩ ($R>h/2e^2$) [53]which was the resistance of single gold atom. Figure 18 illustrated the self-made LabVIEW program.

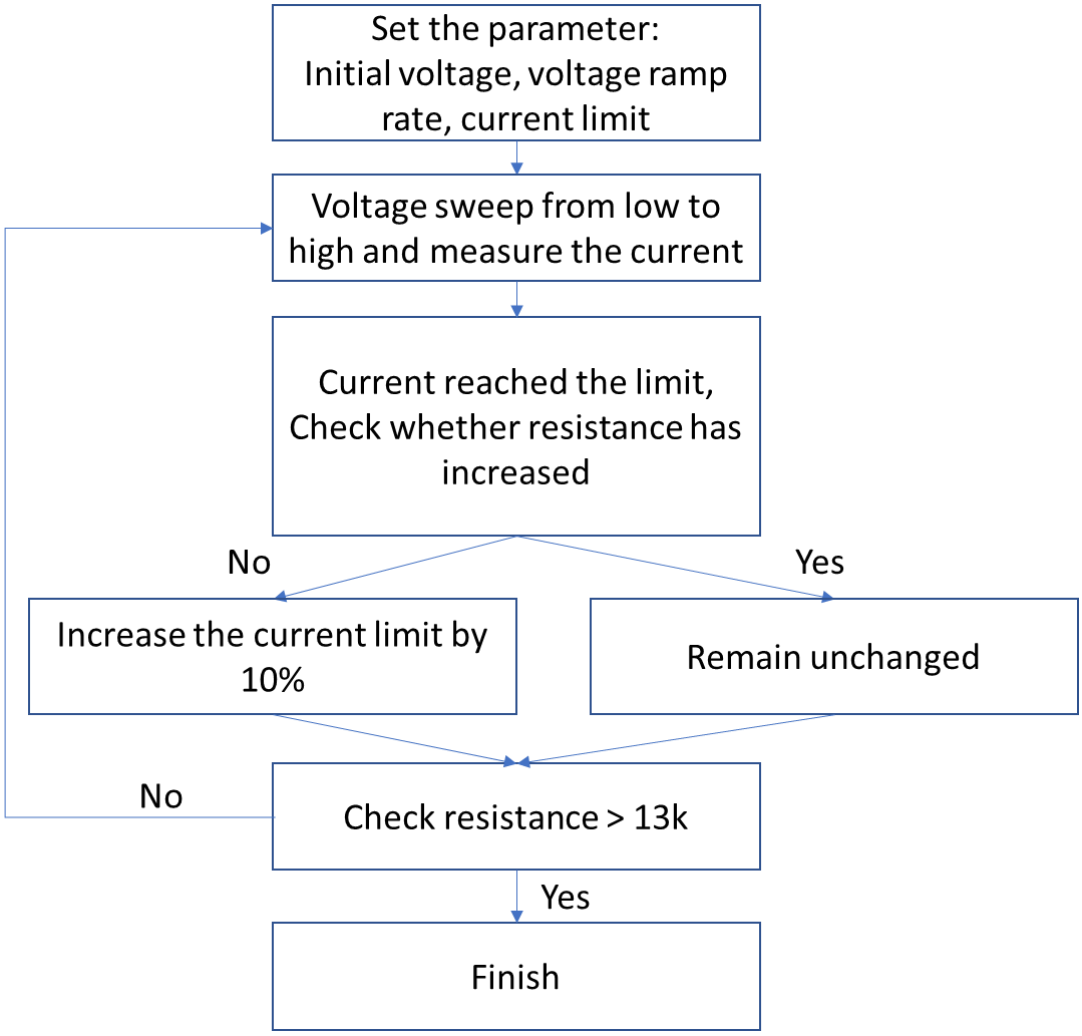

Figure 17. The schematic of process flow of electromigration (current-voltage sweep).

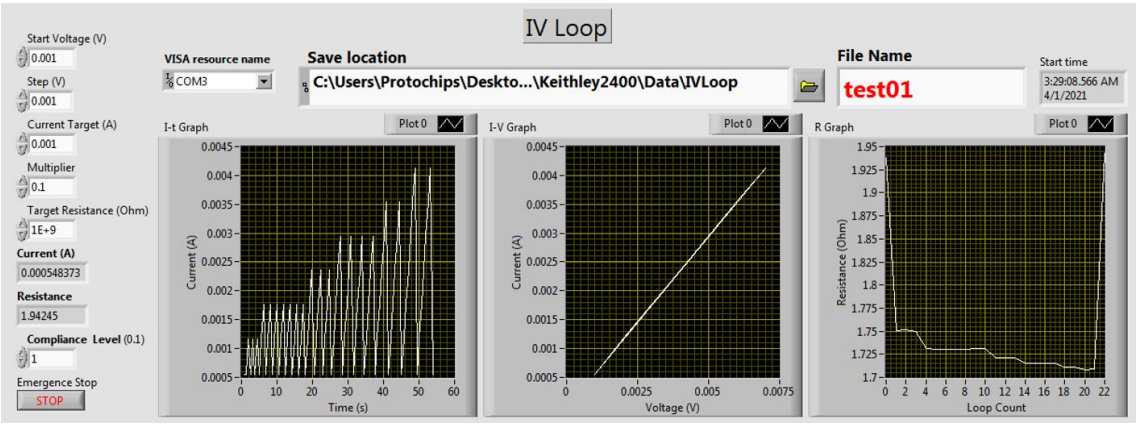

Figure 18. Panel of self-made LabVIEW program for Current-Voltage sweep method.

For resistance feedback methods[54], compared with current-voltage sweep, the process was simplified and more stringent with feedback. To prevent thermal runaway, voltage was not sweep from 0V again but there was feedback in each voltage to control the electromigration. First, Keithley 2400 and self-made LabVIEW (Figure 19) programme applied the initial voltage and measure the resistance. When the resistance reached 13 kΩ, the programme stopped and nanogap was fabricated. When the programme was not stopped as expected, the resistance(R_1) was compared with previous test point(R_0). If $R_1 < R_0$, the voltage was then be increased by 0.01V to measure the resistance again (R_2) until $R_{n+1} > R_n$. After the tests two feedbacks mechanism were concluded. The different between neighbour resistance is larger than 2% and 1%. If it was larger than 2%, voltage was reduced by 85% and resistance was measured again to prevent gold island formation and larger gap due to heat. If the different between neighbour resistance was smaller than 2% but greater than 1%, voltage was reduced by 95% and resistance was measured to ensure slow electromigration process (Figure 19)

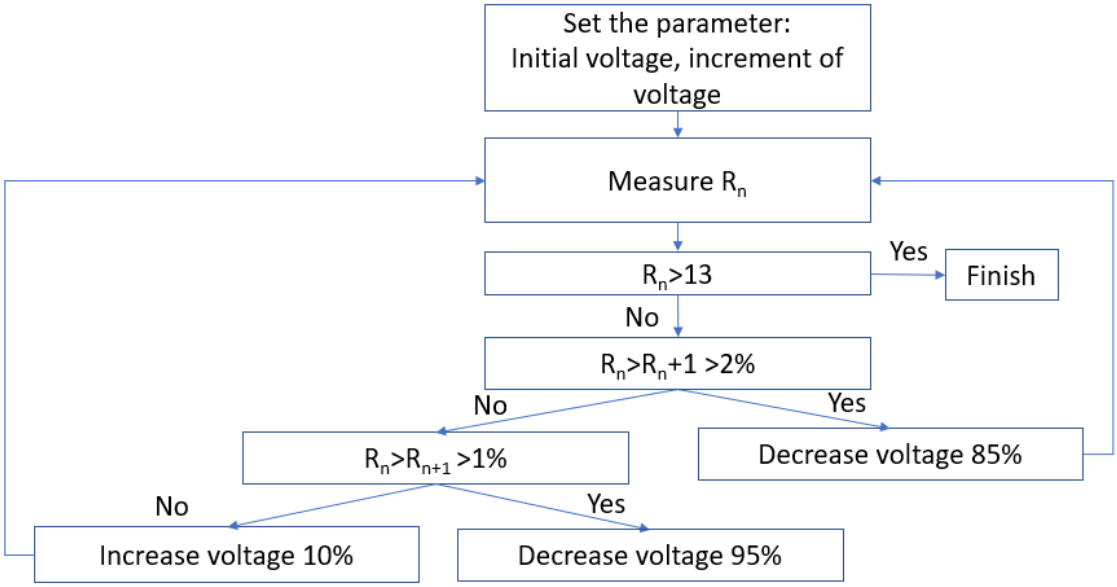

Figure 19. The schematic of process flow of electromigration (resistance feedback).

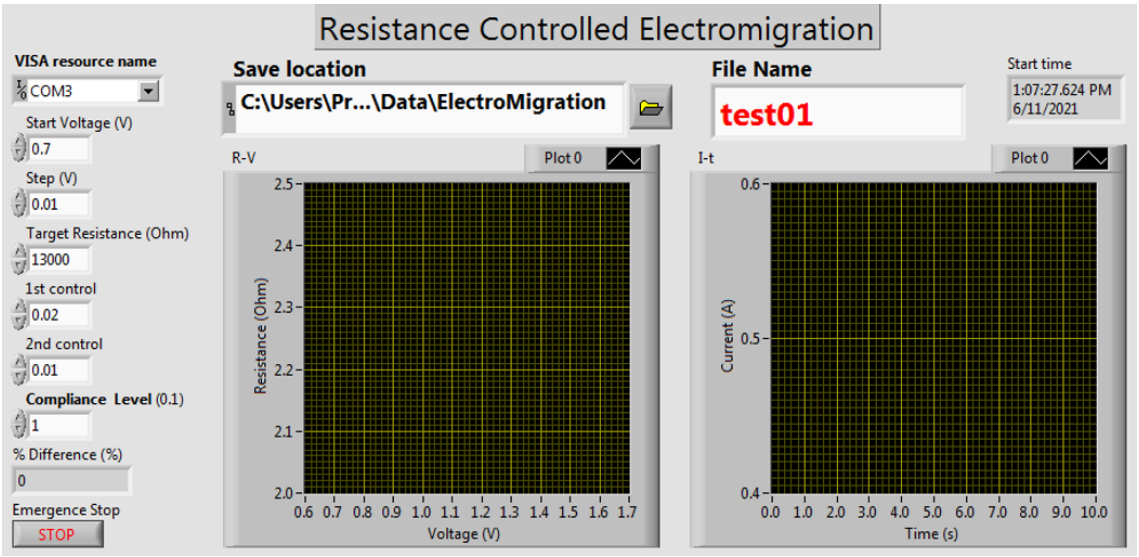

Figure 20. Panel of self-made LabVIEW program for resistance feedback method.

3.1.4. Sensor testing

3.1.4.1. Setup of the PM sensor

PM sensor consists of three parts: measurement unit (keithley 2400) (Figure 21), PM sensor (Figure 23) and flowrate controller (Pump) (Figure 22). First, inserted the sensor chip into the PM sensor case at a 45-degree angle and close to the inlet (Figure24). Then, connected the PM sensor outlet with a gas pipe to the pump. After that, PM sensor was connected to measurement unit, Keithley 2400, controlled by self-design LabVIEW programme to perform current -time measurement. LabVIEW programme controls the Keithley 2400 to apply a constant voltage and measurement. Also, the programme could detect the peak and count the number of the peak in the measurement. In order to increase the measurement speed, the duration of once measurement was limited to less than 100s to achieve 10 count/sec because lack of memory in the Keithley 2400. First, parameter (voltage, sample count, threshold voltage for peak detection) could be entered. The data was stored in Keithley 2400 during testing. After the first test, the data stored in Keithley 2400 was transferred to the computer and showed in the I-T graph and count the peak, then the second test would start immediately. The result showed the morphology of peak and the number of the peak during the testing for further analysis. The sensor was tested in different weather.

Figure 21. Photo of Keithley 2400.

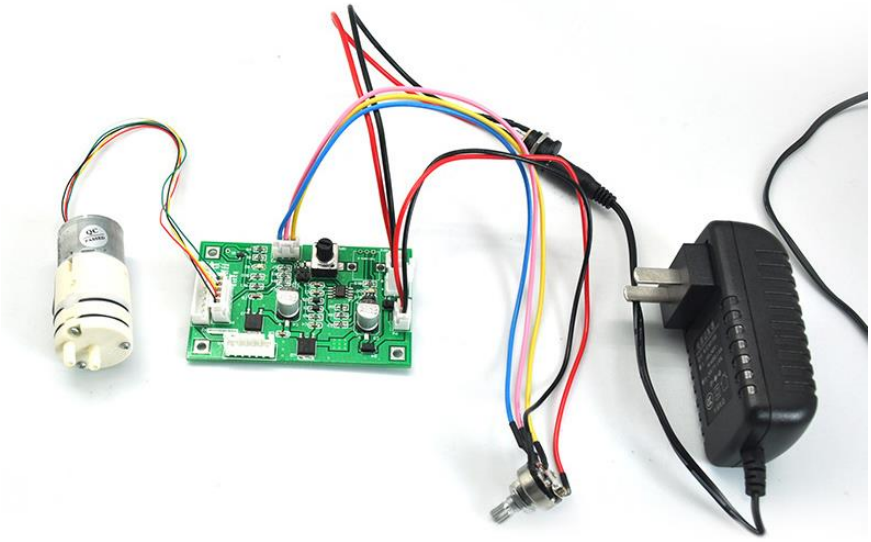

Figure 22. Photo of configuration of the pump.

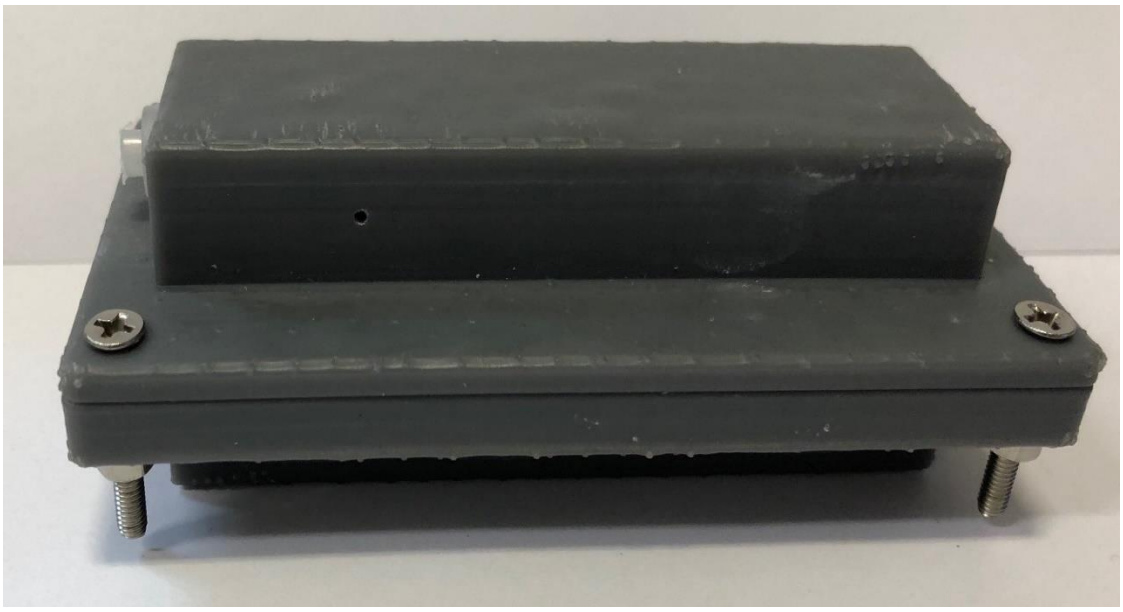

Figure 23. Photo of PM sensor

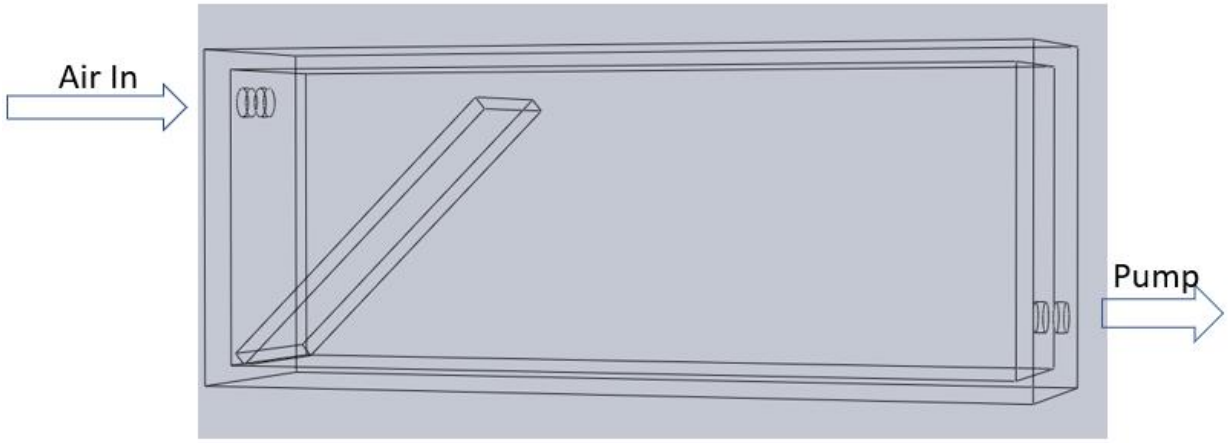

Figure 24. Diagram of PM sensor

3.1.4.2. Particulate matter measurement

Current-time measurement were conducted by Keithley 2400 and self-made Lab-VIEW programme (Figure 25). The constant voltage was set to 1V during the experiment. LabVIEW programme also measured and detected the number of peaks for counting. The resolution of Keithley 2400 was around 1pA and 10count/s after optimization. In order to

improve the measurement speed, the duration of one measurement was limited to less than 100s to achieve 10count/sec due to insufficient memory of Keithley 2400. First, parameter (voltage, sample count, threshold current for peak detection) could be entered. The data was stored in Keithley 2400 during testing. After the first test, the data stored in Keithley 2400 was transferred to the computer and showed in the I-T graph and count the number of peaks based on the threshold current, then the second test would started immediately. The result showed the morphology of peak and the number of the peak during the testing for further analysis. The sensor was tested in different flow rate and different weather.

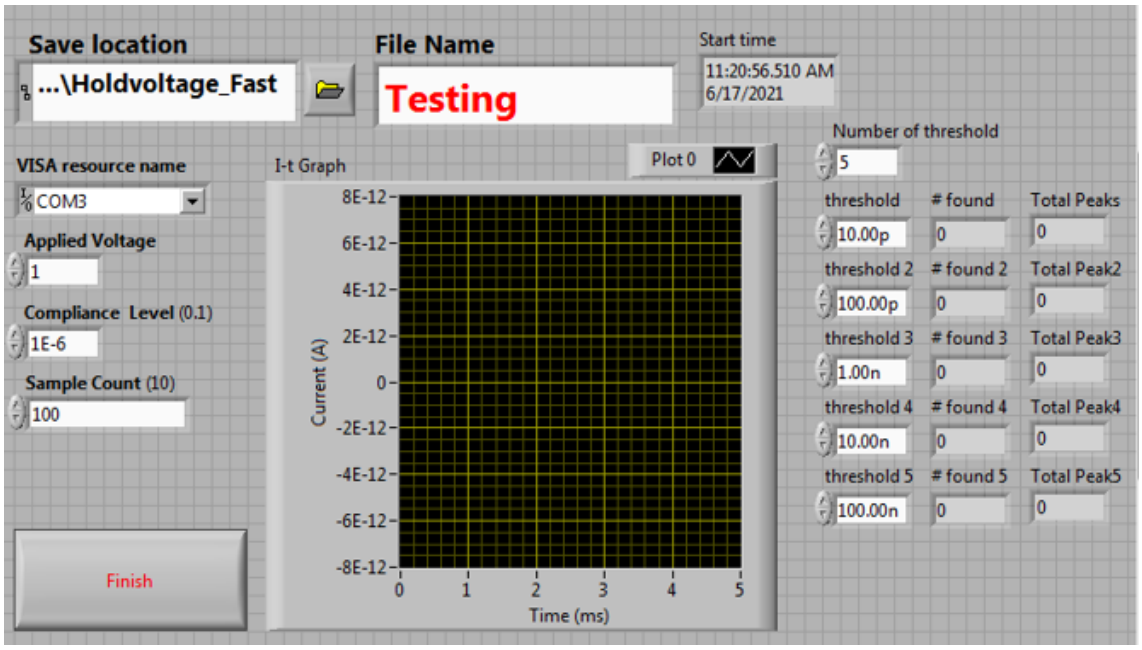

Figure 25. LabVIEW panel of PM measurement.

3.1.4.3. Sample Collection

Particulate matter sensor was tested on the Ground Floor, Hong Kong Polytechnic University in Hung Hom. Hung Hom is one of the heavily trafficked because Hung Hom has the major tunnel connect Hong Kong Island and Kowloon. PM collected was mostly combusted by the vehicle cross the busy road and it is one of the major sources of the PM

in Hong Kong. The collected PM mainly released by the vehicles that crossing the busy roads and it is one of the major sources of PM in Hong Kong. The weather conditions for experiment were recorded (Table 1).

Table 1. The weather conditions for our measurement

	Day 1	**Day 2**	**Day 3**	**Day 4**	**Day 5**
Weather	Sunny	After Heavy Rain	Sunny	Cloudy	Cloudy
Relative Humidity (%)	67.8	73.7	65.9	77.4	71.2
Temperature(ºC)	28.5	25.0	29.4	27.8	29.2

3.1.4.4. Controlled experiment for PM sensor

DT-9880(CEM) was a commercial PM counter by optical sensing and it could distinguish 5 different sizes of the PM which is 0.3um, 1um, 5um, 2.5um and 10um. To compare the result, DT-9880 and PM sensor were used for measurement at the same time. Also, DT-9880 was used to measure relative humidity and temperature for analysis how PM is influenced by the weather.

Chapter 4. Result and Discussion

This section is going to discuss the result of electromigration and the sensor result.

4.1.1. Nanogap fabrication by electromigration

Electromigration was used to fabricate a nanogap electrode on the SiO/Si. To control the experiment, a self-made programme connected to Keithley 2400 needed for the electromigration experiment. 2 different methods were used to compare the result of nanogap electrode, they were Current voltage sweep and resistance-voltage control.

4.1.1.1. Electromigration- Current-Voltage sweep

The sample of electromigration experiment used 1um thin, 5;50nm Cr/Au nanowire (Figure 26). To compare the result (Table 2), 4 different ramp rates (2mV/s, 4mV/s, 20mV/s, 200mV/s) were used to minimize the width of nanogap. The current density before broken was around 8 x 10^{11} A/m^2. Among these 4 slopes, 4mV/s had the best performance, and the width of the gap was the narrowest and high uniformity. In the 4mV/s, 20mV/s (Figure 28D, 29C), the current-voltage (IV) curve performed non-linear behaviour and had a window in the IV curve showed the effect of the electromigration. It was worth notice that although 2mv/s shows electrode breakdown, the morphology in Figure 27A shows that the electrode remains unchanged, and wire connected between the bond pad and the PCB board was separated. For 20mV/s, although the narrow section of the wire was thinner than 4mV/s, the uniformity was extremely low because of the high current density caused the thermal runaway. For 200mV/s, the rapid voltage sweep generated large amount of heat, and caused rapid stress, therefore the width of the gap was

widest. Nanogap (average 80nm) was formed by applying 4mV/s voltage sweep to the wire and the sample could be installed to PCB to further testing.

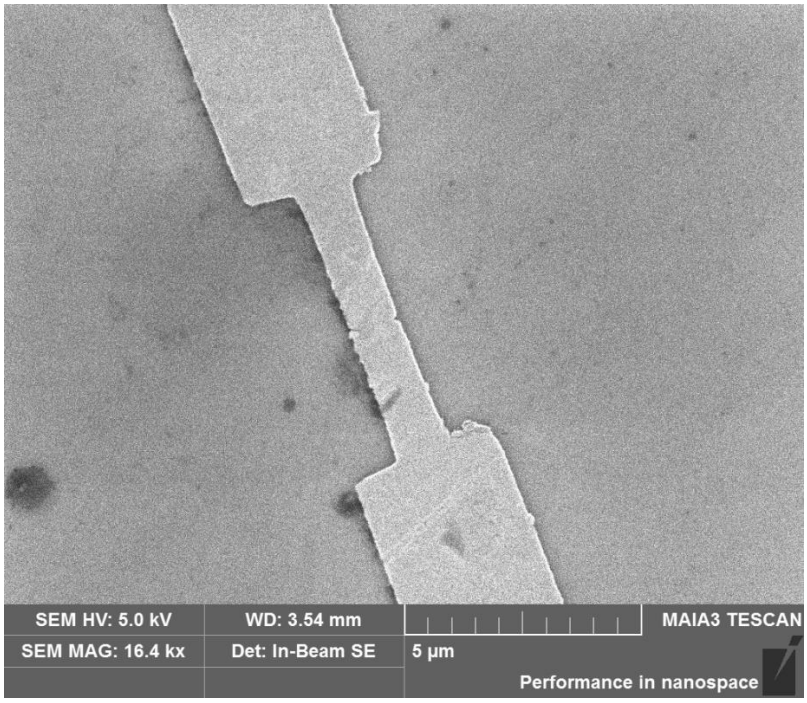

Figure 26. Initial sample for electromigration.

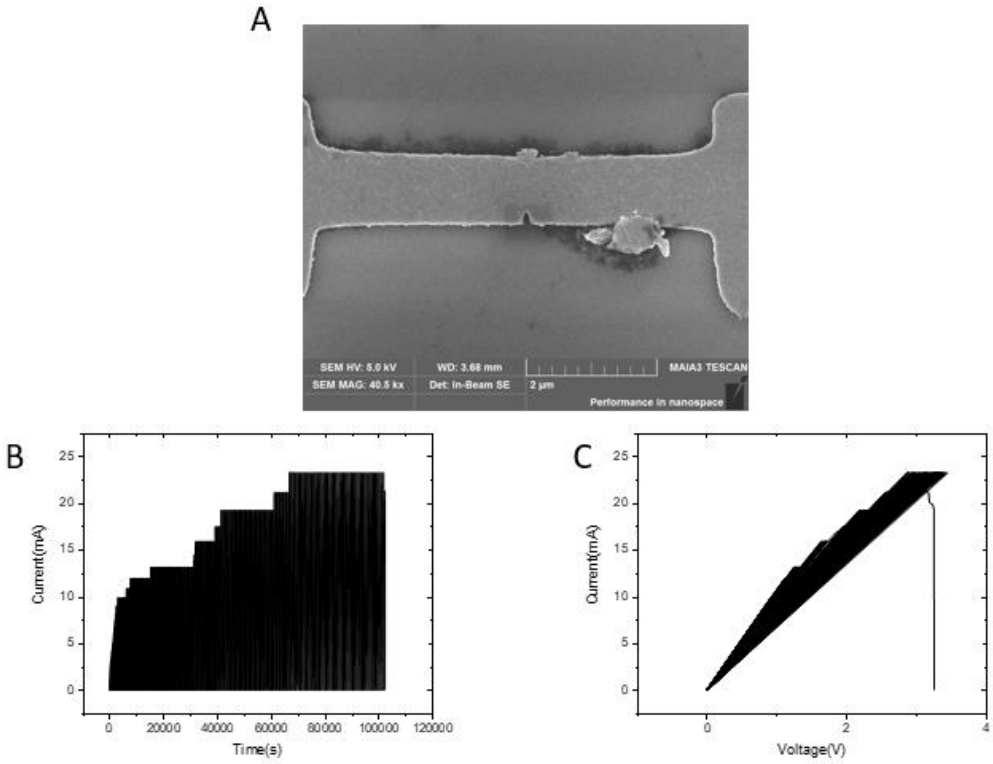

Figure 27. 2mV/s Current Voltage sweep Result. (A) SEM images of result. (B) Current-Time curve for 2mV/s rate. (C) Current- Voltage curve for 2mV/s rate.

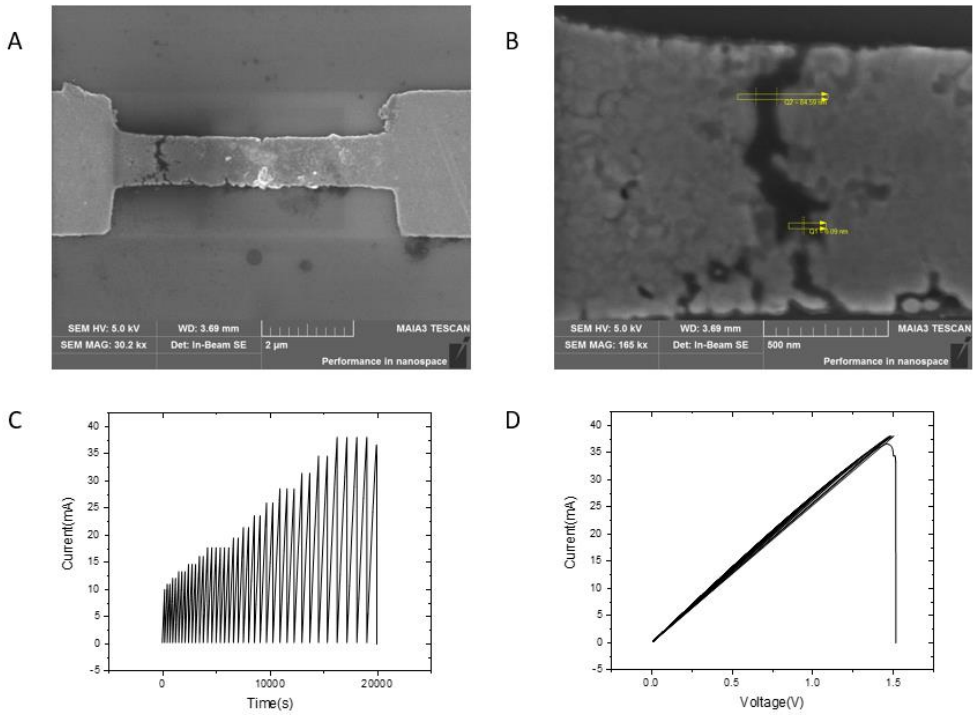

Figure 28. 4mV/s Current Voltage sweep Result. (A,B) SEM images of result. (C) Current-Time curve for 4mV/s rate. (D) Current- Voltage curve for 4mV/s rate.

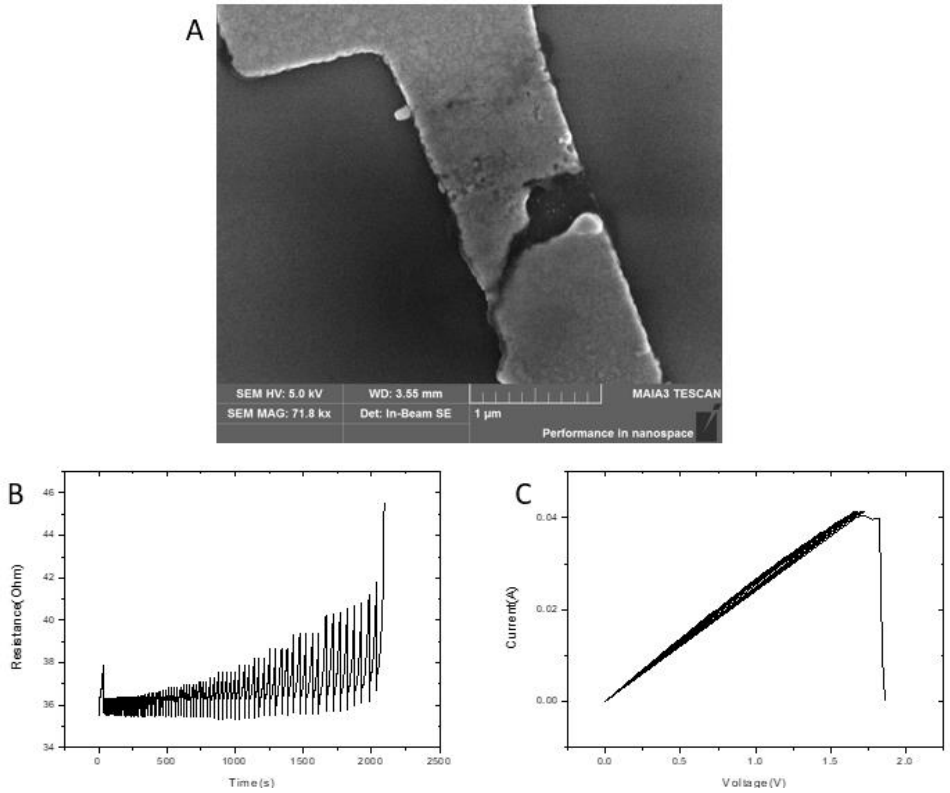

Figure 29. 20mV/s Current Voltage sweep Result. (A) SEM images of result. (B) Current-Time curve for 20mV/s rate. (C) Current- Voltage curve for 20mV/s rate.

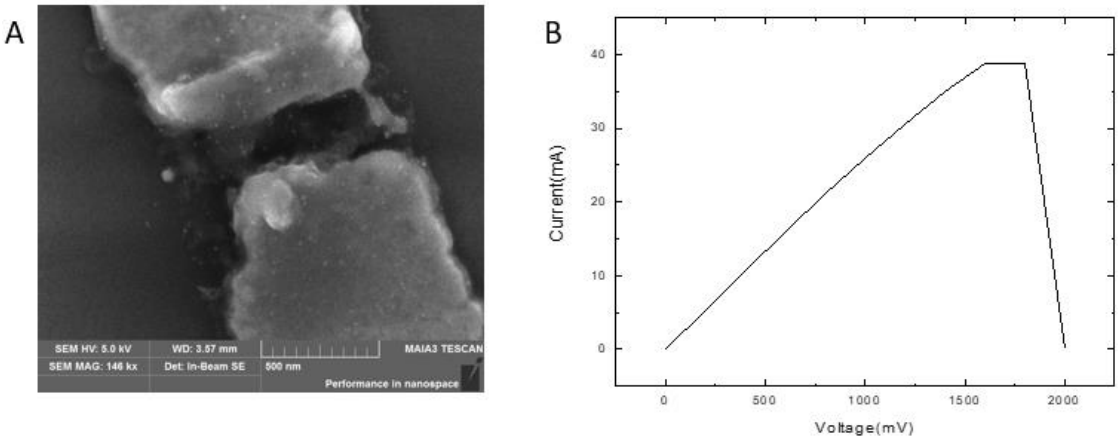

Figure 30. 200mV/s Current Voltage sweep Result. (A) SEM images of result. (B) Current- Voltage curve for 200mV/s rate.

Table 2. Result of nanogap fabrication by current-voltage method

Ramp rate	2mV/s	4mV/s	20mV/s	200mV/s
Uniformity	N/A	Yes	No	Yes
Narrow(nm)	N/A	6.09	59	223
Avenge(nm)	N/A	80	139	300
Current density (A/m^2)	N/A	7.6×10^{11}	8.4×10^{11}	7.8×10^{11}

4.1.1.2. Resistance feedback method for electromigration

Current-Voltage sweep methods consumed a lot of time, the best result (4mV/s) took 5.5 hours to produce one nano gap and the long-time measurement induced large amount of heat to cause the large gap. Also, the width of gold nanowire reduced to decrease the aspect ratio of nanogap fabrication. The sample of electromigration experiment used 500 nm thin, thickness was 5:50nm Cr/Au nanowire. There were 2 set of data varying initial voltage which was 0.1V (Figure 31) and 0.6V (Figure 32). Both got a uniform gap, the avenge width of gap was 63nm and 15nm, the narrow width of nano gap was 17 and 6 respectively. The current density before broken was 1.92×10^{12} A/m^2 and 5×10^{11} A/m^2(Table 3). The higher initial voltage got the narrowest nanogap and lowest current density among of 2 methods. Surprisingly, the highest current density did not produce the largest nanogap and narrower than previously result. It means the current voltage sweep methods induced heat much higher than resistance control method and even overwhelm the effect of high current density.

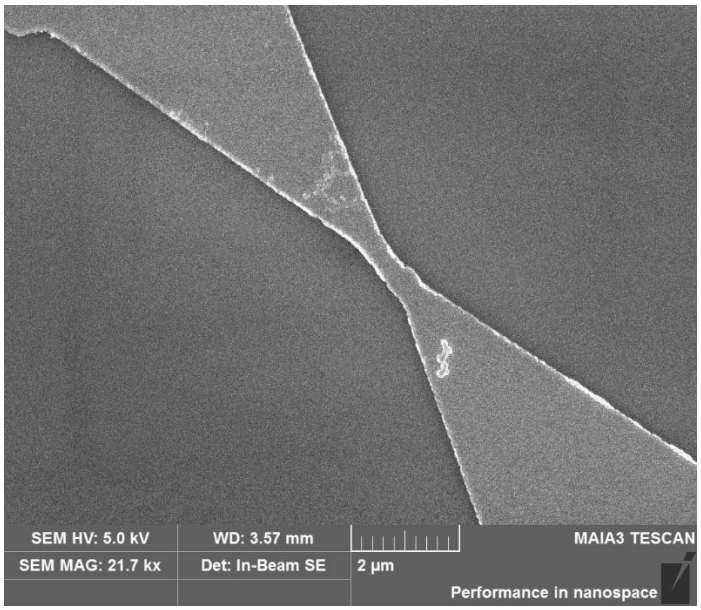

Figure 31. Initial sample for electromigration

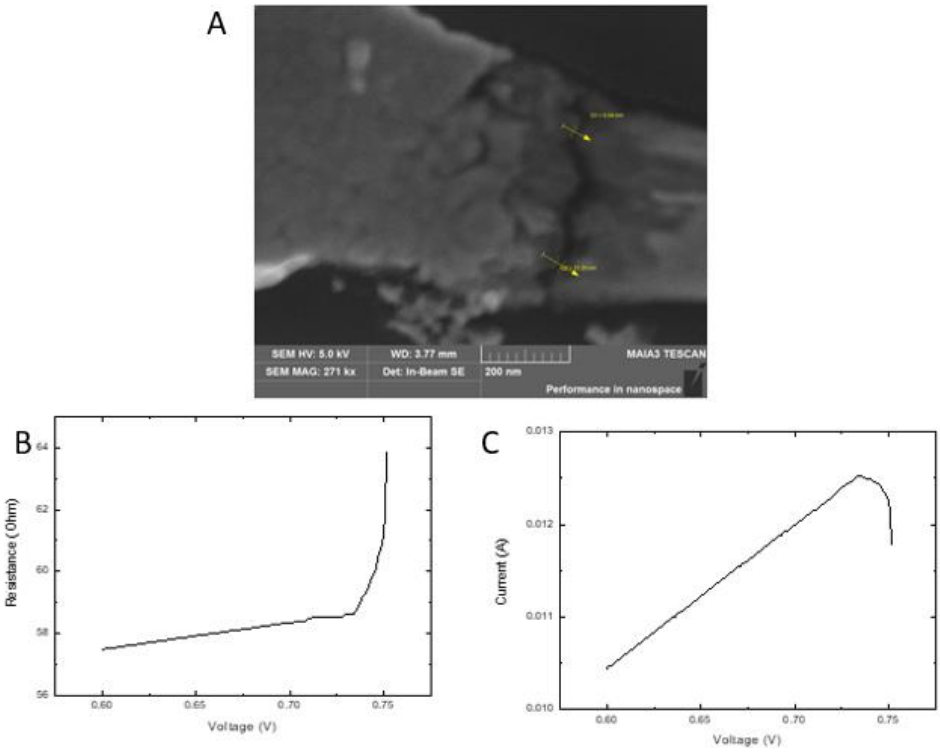

Figure 32. (A) SEM images of result. (B) Resistance-Voltage Curve (C) Current-Voltage curve

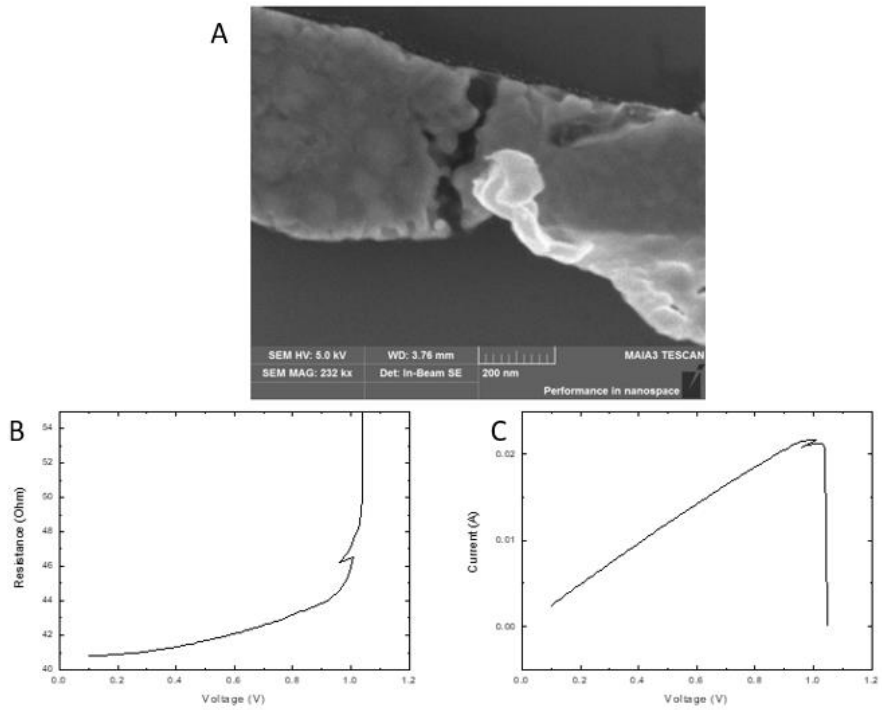

Figure 33. A) SEM images of result. (B) Resistance-Voltage Curve (C) Current-Voltage curve.

Table 3. Result of nanogap fabrication by resistance feedback method

Initial Voltage	0.6V	0.1V
Uniformity	Yes	Yes
Narrow(nm)	6	17
Avenge(nm)	15	63
Current density (A/m^2)	5×10^{11}	1.92×10^{12}

4.1.2. Particulate matter Sensor result

The best result of the two electromigration method was used as a sensor chip and its uniform 80nm nanogap and 15 nm nanogap could measure single PM below 100nm in diameter. The details of measurement information are in Chapter 3. When the single

PM collided the nanogap, current spike was induced, and PM dissolved at an incalculable rate. By this electrical signal, the number of spikes, morphology of spike and amplitude of spike was used to analysis.

4.1.3. Result of uniform 80nm nanogap produced by current voltage sweep method

80nm nanogap device had been tested 5 days. The current-time curve showed the spike which the particulate matter touches the nanogap and closed the circuit. One spike represents one particulate matter connected the nanogap.

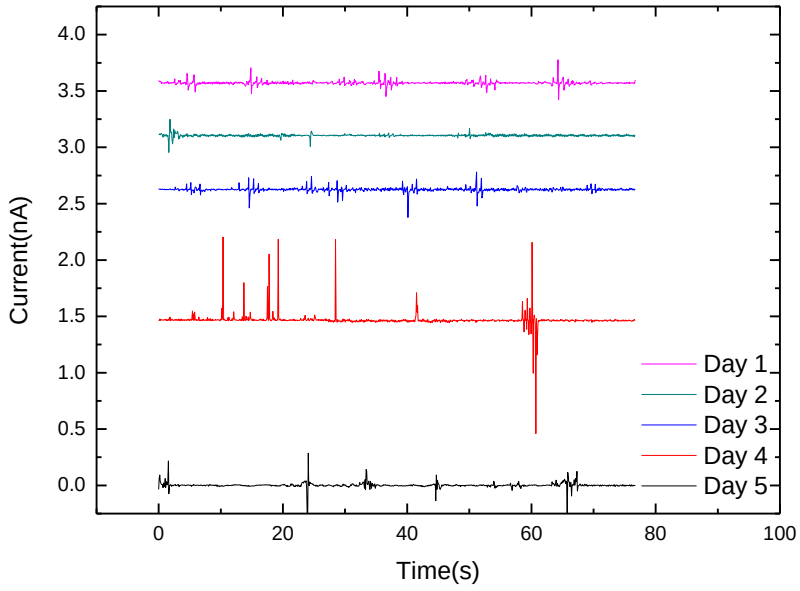

Figure 34. Current-time curve of 15 nm nanogap single PM measurement**.**

For the amplitude of spike, the amplitude of the current was correlated to the size and the composition of the PM. The relationship of the particle size and relative humidity could be defined by hygroscopic growth factor[17].

$$GF(RH) = \frac{D(RH)}{D(DRY)} \quad \textbf{Eq. 4}$$

Where D(RH) was the diameter of RH and D(DRY) is the diameter of PM in dry. Hygroscopic growth factor was the change of the diameter of PM. Therefore, the RH was proportional to the size of PM. Figure 35 shows the amplitude of the spike was comparable to the RH except Day2 because it was a heavy rain during measure and pollution level was expected to be very low on rainy days [17]. On day4, the amplitude of the current was highest which meant the largest size and low resistance of PM. In contrast, on day 3, the amplitude of the current was lowest which meant the smallest size and high resistance of PM. Figure 36 illustrated the relationship between RH and amplitude current is close to linear which fit to eq.4. It is consistent with the size of PM represented by RH and current.

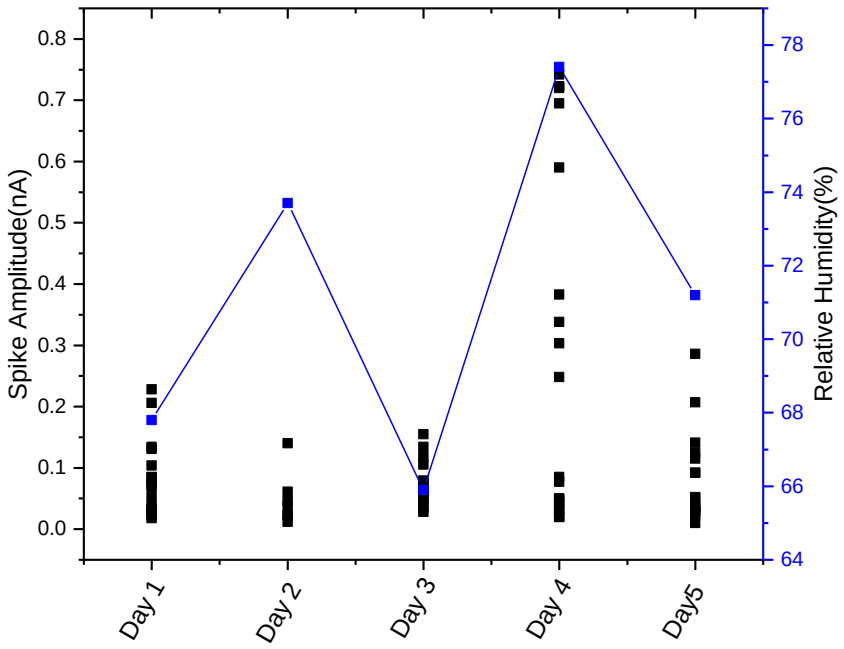

Figure 35. Spike amplitude in different weather condition.

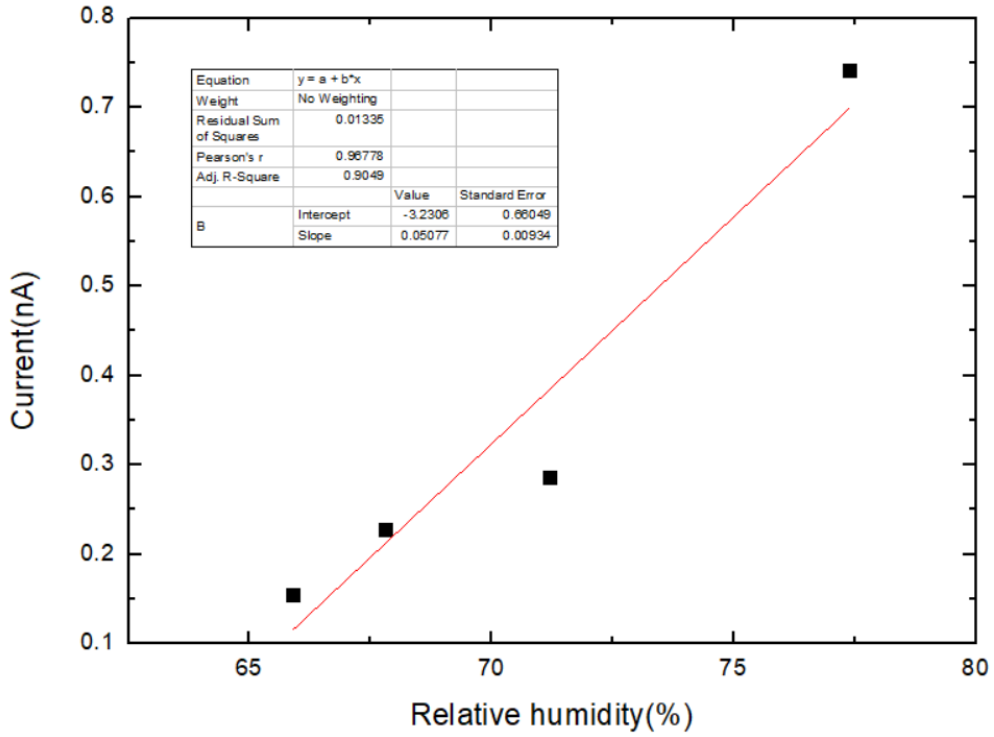

Figure 36. Relative humidity versus current Day 2 is negligent.

For the number of spikes, one spike responded to one single PM collided to the nanogap and measured the flow rate and got the PM concentration of the air. Day 4 had the highest concentration of UFP (Figure 37). There was a contrast in day 4 compared with commercial DT-1880 device. However, Day 4 was a cloudy and the RH was high, which means air pollution was serious in that day. Single PM sensor had a more reliable counting on Day4. also, there were opposite result in Day3 which was a sunny and the RH was low. The measurement of DT-1880 showed that air pollution on day 3 was the most serious among 5 days. In the other hands, the single PM sensor showed the amplitude of current spike was low on day 3 which meant the size of PM should be small. The sunny and low RH had a low level of air pollution because the PM could not intake of water to increase the size. Therefore, it is believed that single PM sensor had a better result for air pollution. However, the exact counting of PM was hard to calculated because

the flow rate and the attractive force by the E-field was non-negligible. In this step, single PM sensor could only demonstrate the ratio of number of PM in different weather.

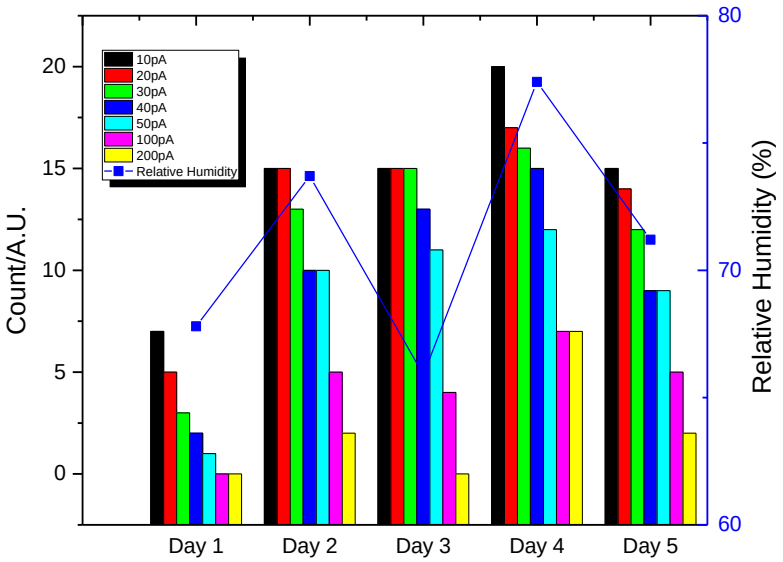

Figure 37. Count of number of spikes in different weather condition.

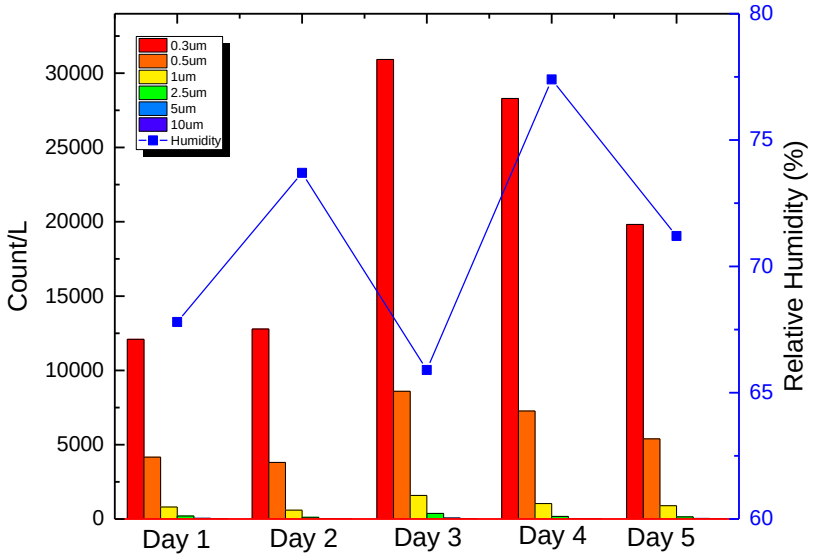

Figure 38. Count the number of PM by DT-9880(CEM)

Before analysis the morphology of the spike, resistor(R)-inductor(L)-capacitor(C) circuit (RLC) circuit should be introduced (figure). Using Kirchoff's Voltage law,

$$v_r + v_l + v_c = v_s \qquad \textbf{Eq. 5}$$

Where v_r is the voltage drop by resistor ,v_l is the voltage drop by the inductor, and v_c is the voltage drop by the capacitor and v_s is the power supply. By expends and differentiation.

$$R\frac{di}{dt} + L\frac{d^2i}{dt^2} + \frac{i}{C} = 0 \qquad \textbf{Eq. 6}$$

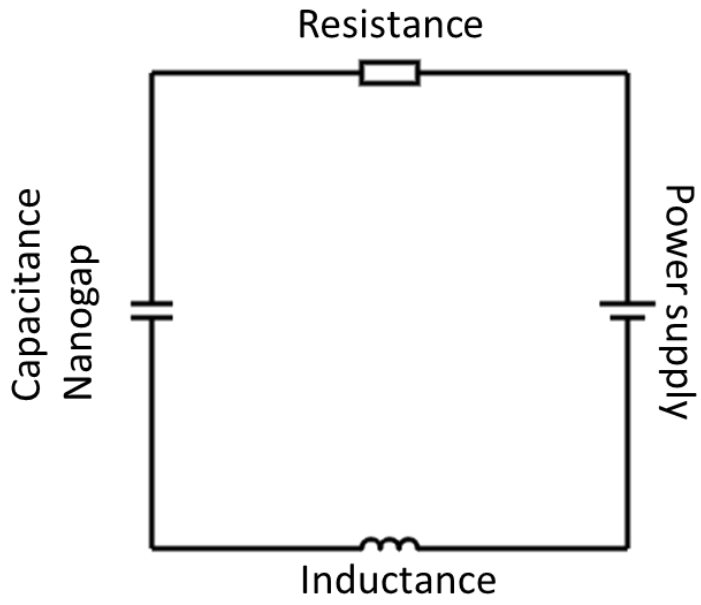

Figure 39. Schematic diagram of RLC circuit

Damping factor (ζ) is used to determine the circuit response. Depending on the constant of resistance, inductance and capacitance, there are three different types of response excited by the power supply which is overdamped ($\zeta > 1$), critically damped ($\zeta = 1$)or underdamped($\zeta < 1$) and show different morphology of the current spike.

$$\zeta = \frac{\alpha}{\omega_0} = \frac{\frac{R}{2L}}{\frac{1}{\sqrt{LC}}} \qquad \textbf{Eq. 7}$$

where α is attenuation and ω_0 is the resonance frequency. Overdamped response is a decay of current spike without oscillation. Underdamped response is a sine decays oscillation signal. The envelope of the oscillation can be described by attenuation(α). Critically damped response is the fastest decay of a current spike without oscillation. The type of particulate matter can be recognized by the morphology of the spike and confirmed by TEM images.

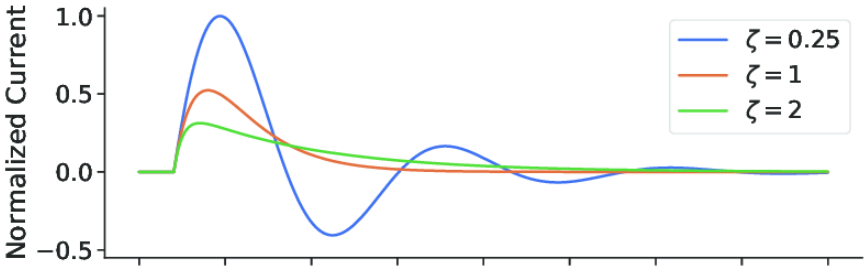

Figure 40. Current-time curve of relationship between damping factor and morphology

First, from the current-time curve (Figure 34), different types of signals were detected which can divided to 3 main types: spike with one rebound (Figure 41), spike with a sine decay oscillation (Figure 42) and spike without oscillation (Figure 42). In Figure

41, the underdamped ($\zeta < 1$) solution (eq.8) is used to fit the signal. Small attenuation ($\alpha = 10.10$) is calculated by the envelope of the oscillation (eq.9) with low resistance is predicted. Inorganic metal with metals ion (Fe, Mn, Ca, Zn) have the similar characteristics and match the high RH weather condition. Second, the spike with sine decay oscillation is also fitted by underdamped solution. The attenuation of the signal shown in Figure 42 is 21.978 and higher than the precious inorganic particles signal. Onion-shaped caron soot can be found in the dry day and mainly contains carbon.

$$I(t) = Be^{-\alpha t}\sin(\omega t + \varphi) \quad \textbf{Eq. 8}$$

$$\ln(I) = -\alpha + \ln(I_o) \quad \textbf{Eq. 9}$$

Third, the signal of the sharp spike without oscillation can be found in raining day. High salt particles collide with the nanogap as a pure resistance like a water dropped in a channel. Therefore, the size of the particles is large, and the resistance should be the smallest. The secondary organic aerosols may match the sharp spike signal because of the high water-intake and high salt ion (Cl, Na, K, S, O). Also, this type of signals usually has high current amplitude and sharp decays. The amplitude and the size of the particles and water in-take affect may have a co-relation. However, it is difficult to simulate a real high water in-take PM to find the relationship between the particles and the signal. Nowadays, the research of the calibration sensor is using simulated volatile organic compounds which is the organic chemicals vapors in ambient temperature. After the calibration, the size and the characteristic of the particulate matter can be estimated by this sensor.

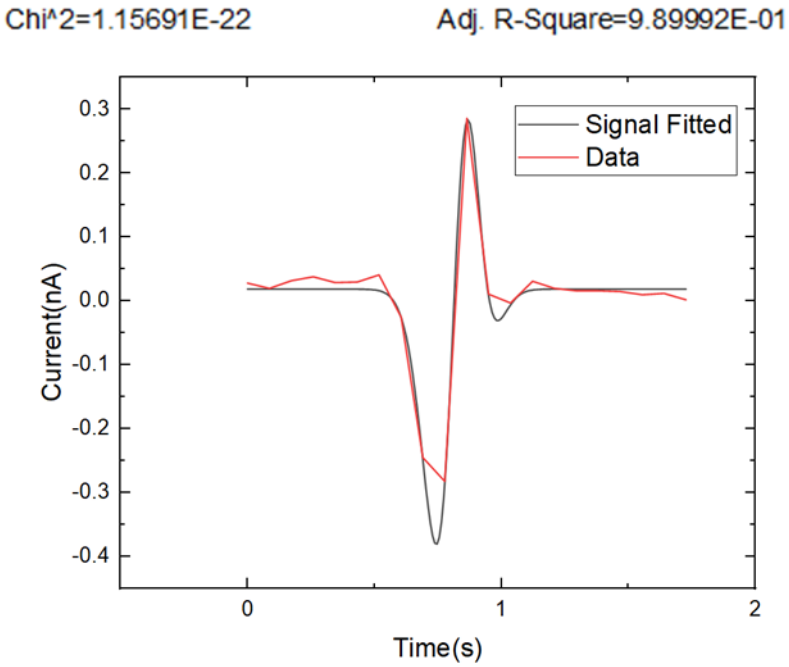

Figure 41. Current-time curve of the spike with rebound feedback

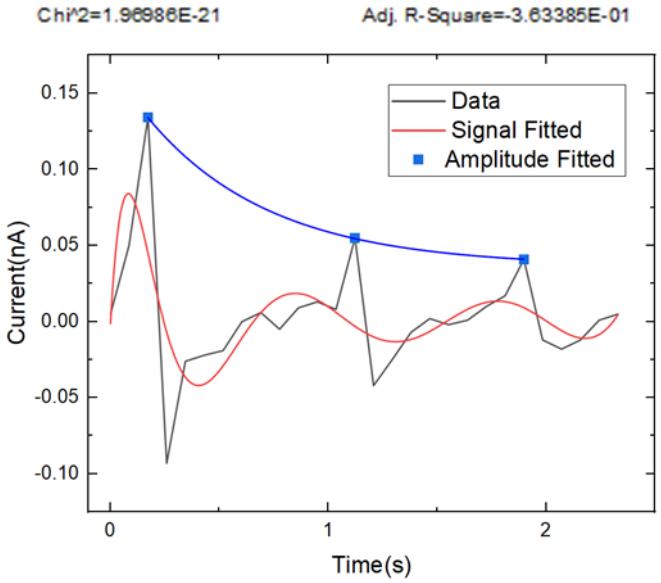

Figure 42. Current-time curve of spike with a sine decay oscillation

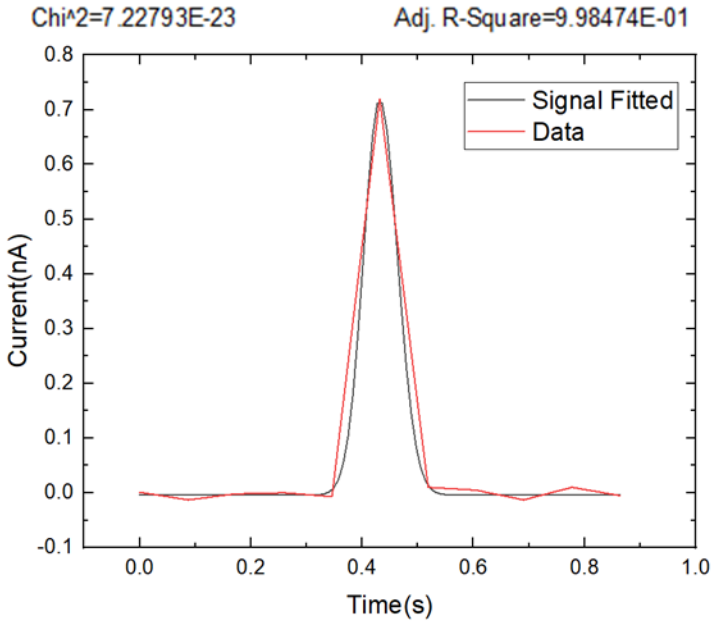

Figure 43. Current time curve of a sharp spike without oscillation

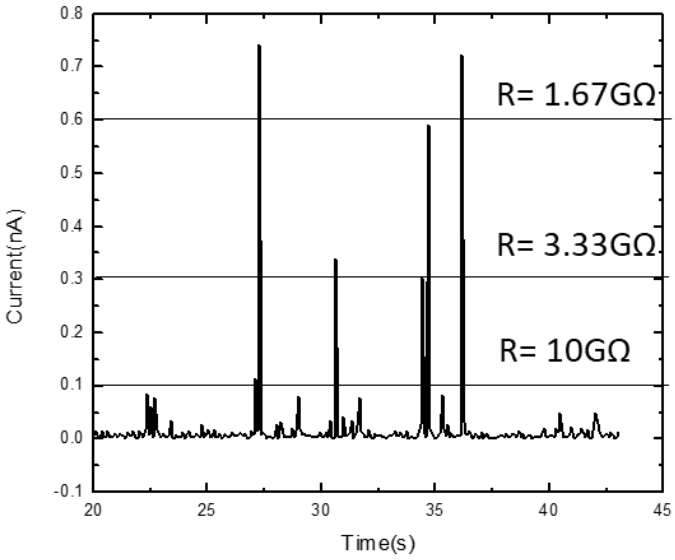

Figure 44. Current-time curve of raining day

To fulfil the three sensor criteria which is sensitivity, selectivity, and stability, Nanogap device had a sensitivity and selectivity of single SAs by electrical measurement which can measure UFP. Narrower nanowire can produce further narrow nanogap and Previous research has demonstrated that reducing the gap separation between the electrode pairs improves the device's sensitivity [50, 52], limit of detection[45], and response speed. However, the narrow nanogap cannot adopt a PM collision. Therefore, the stability was limited to the strength of the nanogap. There are several failure mechanisms of nanogap: Chromium metal dissolved, electrodialysis and ion exchange. The bottom metal chromium may have an electrochemical reaction to different ion in high water-intake particle. Also, Nanogap may be destroyed by the collision of PM (Figure 45-46). The first priority of being commercial sensor is to require sufficient strength to perform long time measurement.

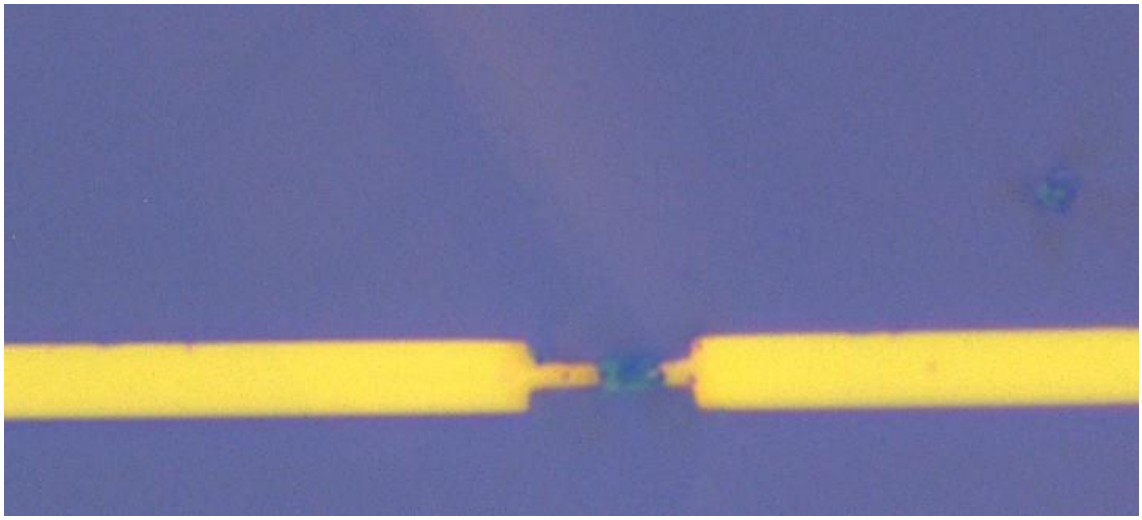

Figure 45. The optical microscopy photos of nanogap after 5days measurement.

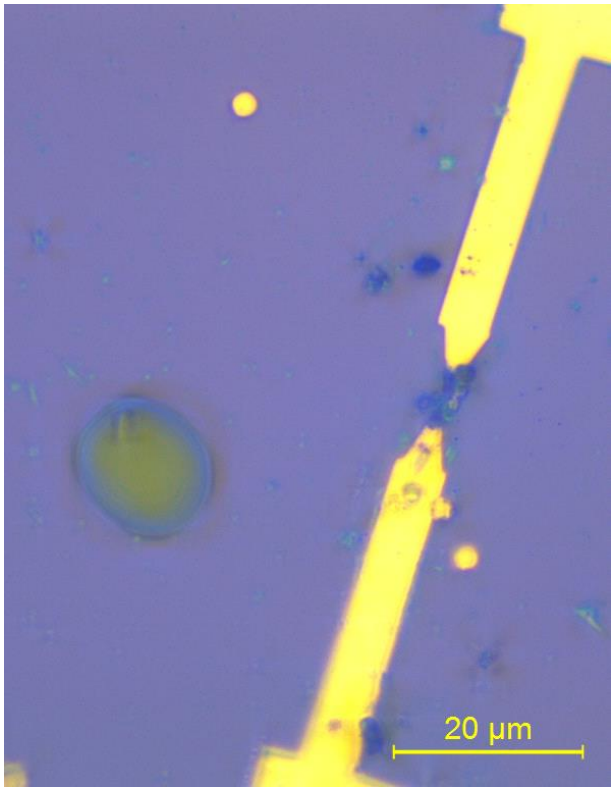

Figure 46. OM photos of resistance feedback's device after one measurement

Chapter 5. Conclusion and Prospective

. The alarming situation of air pollution in China has drawn great attention from all around the world to understand the effect of particulate matter especially the most toxic UFP[55]. The composition and structure model were investigated by TEM and STEM-EDS[20]. The next step for this research area should be focusing on the measurement of sensing UFP in real time due to the limitations of current sensor.

To conclude, this research aimed to construct a new electrical sensing method for detecting UFP, lack of real-time measurement of most toxic UFP is a challenge in research field. The technology of nanogap sensing was used to be a sensor for example, H_2, NO, especially in biological sensor for DNA. After established nanogap technique, it is time to measure single UFP by nanogap metal-particle-metal configuration in real time measurement. This work used two different electromigration methods (current voltage sweep and resistance feedback method) to produce <100nm nanogap for single UFP measurement. The five days experiment experienced different weather from high RH to low RH and it is comparable to theory of PM based on the analysis of the current spike (counting the number of spikes, morphology of spike and amplitude of current). The amplitude of current match the linearly hygroscopic growth factor based on the relative humidity. The core shell structure of hygroscopic SAs act as sphere capacitor also fit the morphology of current spike to define the composition of SAs in real time. Therefore, It can be concluded that this work starts a new chapter for sensing UFP.

To be a commercial sensor, there are some shortcomings of this single PM sensor needed to be solved first. There are two problem of this PM sensor which is durability of the sensor and the exact counting of PM. The durability is contradicted with the nanogap

measurement. The reduction of gap increased the resolution of the measurement and respond speed and easy to break by collision of PM unless the much longer nanogap can be produced or reduce the force of collision of PM. Also, the disadvantage of counting problem can be solved by finite element simulation to calculate the flow rate on the nanogap. Nevertheless, the first step of UFP measurement by nanogap have been introduced in this work.

Reference

1. Y. Lin, J. Zou, W. Yang and C.-Q. Li, Int J Environ Res Public Health **15** (3), 438 (2018).
2. Y. Xie, H. Dai, Y. Zhang, Y. Wu, T. Hanaoka and T. Masui, Environment International **130**, 104881 (2019).
3. A. Mukherjee and M. Agrawal, Environmental Chemistry Letters **15** (2), 283-309 (2017).
4. J. A. Schwab and M. Zenkel, Laryngoscope **108** (1 Pt 1), 120-124 (1998).
5. Y.-F. Xing, Y.-H. Xu, M.-H. Shi and Y.-X. Lian, J Thorac Dis **8** (1), E69-E74 (2016).
6. A. Chung, D. P. Y. Chang, M. J. Kleeman, K. D. Perry, T. A. Cahill, D. Dutcher, E. M. McDougall and K. Stroud, Journal of the Air & Waste Management Association **51** (1), 109-120 (2001).
7. W.H.O, (2016).
8. A. J. Cohen, M. Brauer, R. Burnett, H. R. Anderson, J. Frostad, K. Estep, K. Balakrishnan, B. Brunekreef, L. Dandona, R. Dandona, V. Feigin, G. Freedman, B. Hubbell, A. Jobling, H. Kan, L. Knibbs, Y. Liu, R. Martin, L. Morawska, C. A. Pope, III, H. Shin, K. Straif, G. Shaddick, M. Thomas, R. van Dingenen, A. van Donkelaar, T. Vos, C. J. L. Murray and M. H. Forouzanfar, The Lancet **389** (10082), 1907-1918 (2017).
9. C. Guerreiro, A. González Ortiz, F. d. Leeuw, M. Viana, A. Colette and A. European Environment, (2018).
10. W.H.O, (2015).
11. E. E. McDuffie, R. V. Martin, J. V. Spadaro, R. Burnett, S. J. Smith, P. O'Rourke, M. S. Hammer, A. van Donkelaar, L. Bindle, V. Shah, L. Jaeglé, G. Luo, F. Yu, J. A. Adeniran, J. Lin and M. Brauer, Nature Communications **12** (1), 3594 (2021).
12. Y. Wang, G. Tang, W. Zhao, Y. Yang, L. Wang, Z. Liu, T. Wen, M. Cheng, Y. Wang and Y. Wang, Atmospheric Environment **224**, 117325 (2020).
13. N. A. H. Janssen, J. Schwartz, A. Zanobetti and H. H. Suh, Environ Health Perspect **110** (1), 43-49 (2002).
14. I. Kloog, B. Ridgway, P. Koutrakis, B. A. Coull and J. D. Schwartz, Epidemiology **24** (4), 555-561 (2013).
15. D. E. Schraufnagel, Experimental & Molecular Medicine **52** (3), 311-317 (2020).
16. C. Terzano, F. Di Stefano, V. Conti, E. Graziani and A. Petroianni, Eur Rev Med Pharmacol Sci **14** (10), 809-821 (2010).
17. H.-S. Kwon, M. H. Ryu and C. Carlsten, Experimental & Molecular Medicine **52** (3), 318-328 (2020).
18. J. O. Anderson, J. G. Thundiyil and A. Stolbach, J Med Toxicol **8** (2), 166-175 (2012).
19. X. Fan, W. Zheng and D. J. Singh, Light: Science & Applications **3** (6), e179-e179 (2014).
20. F. Zheng, W. C. Lam, K. H. Lai, L. Huang, L. W. Wong, Y. Zhang, Z. Yan, C. C. Sham, Q. H. Thi, T. H. Ly and J. Zhao, Environmental Science & Technology Letters **7** (8), 560-566 (2020).

21. T. Sasaki, H. Sawada, F. Hosokawa, Y. Kohno, T. Tomita, T. Kaneyama, Y. Kondo, K. Kimoto, Y. Sato and K. Suenaga, Journal of Electron Microscopy **59** (S1), S7-S13 (2010).
22. W. Xu, J. H. Dycus, X. Sang and J. M. LeBeau, Ultramicroscopy **164**, 51-61 (2016).
23. M. L. Trouwborst, S. J. van der Molen and B. J. van Wees, Journal of Applied Physics **99** (11), 114316 (2006).
24. W. Shao, H. Zhang and H. Zhou, Sensors **17** (5), 1033 (2017).
25. T. Njalsson and I. Novosselov, J Aerosol Sci **119**, 1-12 (2018).
26. A. Nagy, W. W. Szymanski, P. Gál, A. Golczewski and A. Czitrovszky, J Aerosol Sci **38** (4), 467-478 (2007).
27. Y. Zheng, F. Liu and H.-P. Hsieh, in *Proceedings of the 19th ACM SIGKDD international conference on Knowledge discovery and data mining* (Association for Computing Machinery, Chicago, Illinois, USA, 2013), pp. 1436–1444.
28. Y. Wang, J. Li, H. Jing, Q. Zhang, J. Jiang and P. Biswas, Aerosol Science and Technology **49** (11), 1063-1077 (2015).
29. A. Ungut, G. Grehan and G. Gouesbet, Appl. Opt. **20** (17), 2911-2918 (1981).
30. in *Absorption and Scattering of Light by Small Particles* (1998), pp. 82-129.
31. M. Fierz, H. Burtscher, P. Steigmeier and M. Kasper, (SAE International, 2008).
32. F. Concas, J. Mineraud, E. Lagerspetz, S. Varjonen, X. Liu, K. Puolamäki, P. Nurmi and S. Tarkoma, *Low-Cost Outdoor Air Quality Monitoring and Sensor Calibration: A Survey and Critical Analysis*. (2021).
33. M. Fierz, C. Houle, P. Steigmeier and H. Burtscher, Aerosol Science and Technology **45** (1), 1-10 (2011).
34. R. Sorbello, Journal of Physics C: Solid State Physics **51**, 159-231 (1998).
35. J. R. Black, Proceedings of the IEEE **57** (9), 1587-1594 (1969).
36. E. Yantac, A. Coskun, M. Fjeld and M. A. Baytaş, *Appreciating Digital Materials for Longevous Computational Artifacts*. (2019).
37. D. R. Strachan, D. E. Smith, D. E. Johnston, T. H. Park, M. J. Therien, D. A. Bonnell and A. T. Johnson, Applied Physics Letters **86** (4), 043109 (2005).
38. T. Li, W. Hu and D. Zhu, Advanced Materials **22** (2), 286-300 (2010).
39. J. Moreland and J. W. Ekin, Journal of Applied Physics **58** (10), 3888-3895 (1985).
40. M. A. Reed, C. Zhou, C. J. Muller, T. P. Burgin and J. M. Tour, Science **278** (5336), 252-254 (1997).
41. J. Xiang, B. Liu, S.-T. Wu, B. Ren, F.-Z. Yang, B.-W. Mao, Y. Chow and Z.-Q. Tian, Angewandte Chemie (International ed. in English) **44**, 1265-1268 (2005).
42. J. G. Fleming, Patent No. US 6503409 United States SNL English (2003).
43. P. Motto, A. Dimonte, I. Rattalino, D. Demarchi, G. Piccinini and P. Civera, Nanoscale Research Letters **7** (1), 113 (2012).
44. M. Tsutsui, S. Rahong, Y. Iizumi, T. Okazaki, M. Taniguchi and T. Kawai, Scientific Reports **1** (1), 46 (2011).
45. Q. Zhao, J. Shao, H. Tian, X. Li, C. Wang and J. Liu, Sensors and Actuators B: Chemical **270**, 475-481 (2018).
46. S. Shukla, P. Zhang, H. J. Cho, S. Seal and L. Ludwig, Sensors and Actuators B: Chemical **120** (2), 573-583 (2007).
47. F. Favier, E. C. Walter, M. P. Zach, T. Benter and R. M. Penner, Science **293** (5538), 2227-2231 (2001).
48. S. Benedict, P. Basu and N. Bhat, Journal of Micromechanics and Microengineering **27**, 075024 (2017).

49. T. T. Phan, T. Tosa and Y. Majima, Sensors and Actuators B: Chemical **343**, 130098 (2021).
50. J. Tamaki, A. Miyaji, J. Makinodan, S. Ogura and S. Konishi, Sensors and Actuators B: Chemical **108** (1), 202-206 (2005).
51. Q. N. Minh, H. D. Tong, A. Kuijk, F. van de Bent, P. Beekman and C. J. M. van Rijn, RSC Advances **7** (79), 50279-50286 (2017).
52. L. Francioso, P. Creti, M. C. Martucci, S. Capone, A. Taurino, P. Siciliano and C. D. Pascali, Proceedings **2** (13), 1027 (2018).
53. A. Yanson, G. Rubio-Bollinger, H. E. Brom, N. Agrait and J. van Ruitenbeek, Nature **395**, 783 (1998).
54. S. Talukder, A. Ghosh and R. Pratap, Journal of ISSS (INSTITUTE OF SMART STRUCTURES AND SYSTEMS) **1**, 16-22 (2012).
55. H. Xu, S. S. H. Ho, J. Cao, B. Guinot, H. Kan, Z. Shen, K. F. Ho, S. Liu, Z. Zhao, J. Li, N. Zhang, C. Zhu, Q. Zhang and R. Huang, Scientific Reports **7** (1), 41132 (2017).